Whole genome duplication through mitotic slippage causes nuclear instability

Gemble S[1,*], Budzyk M[1], Simon A[1], Lambuta R[2,3], Weiss N[4], Forest A[4], Miroshnikova YA[5], Scotto Di Carlo F[1], Marthiens V[1], Verdel C[1], Fang J[6,7], Desdouets C[6,7], Wickström SA[8,9], Ciriello G[10], Oricchio E[2], Almouzni G[4] & Basto R[1,*].

Author affiliations

1. Biology of Centrosomes and Genetic Instability, Institut Curie, Centre National de la Recherche Scientifique (CNRS), Unité Mixte de Recherche 144, Université Paris Sciences et Lettres (PSL Research University), Paris, France.
2. Swiss Institute for Experimental Cancer Research (ISREC), School of Life Sciences, EPFL, Switzerland.
3. Present address: Institute of Molecular Biology, Mainz, Germany.
4. Chromatin dynamics, Institut Curie, Centre National de la Recherche Scientifique (CNRS) Unité Mixte de Recherche 3664, Université Paris Sciences et Lettres (PSL Research University), University, Sorbonne Université, Paris, France.
5. Max Planck Research Group Biophysical Regulation of Cell State Dynamics, Max Planck Institute for Molecular Biomedicine, 48149 Münster, Germany.
6. Centre de Recherche des Cordeliers, Sorbonne Université, INSERM, Université de Paris, Paris, France.
7. Genomic Instability, Metabolism, Immunity and Liver Tumorigenesis laboratory, Equipe Labellisée LIGUE 2023, Paris, France.
8. Department of Cell and Tissue Dynamics, Max Planck Institute for Molecular Biomedicine, 48149 Münster, Germany.
9. Stem Cells and Metabolism Research Program, Faculty of Medicine, University of Helsinki, 00290 Helsinki Finland.
10. Department of Computational Biology, University of Lausanne (UNIL), Switzerland.

* Corresponding author: renata.basto@curie.fr and simon.gemble@curie.fr

Contact information

Correspondence: renata.basto@curie.fr and simon.gemble@curie.fr

Abstract

Whole-genome duplication (WGD), leading to polyploidy can arise in physiological and pathological contexts[1–5]. WGD can occur via non-canonical cell cycles such as mitotic slippage, cytokinesis failure or endoreplication[1,3]. Whether the routes to WGD influence the behaviour of the resulting polyploid cells remains unclear. Here, we compared these routes under both physiological and non-physiological conditions. Remarkably, only mitotic slippage led to widespread nuclear abnormalities defined by highly variable nuclear deformations that we termed nuclear instability. Mechanistically, we found that these nuclei were softer - due to high levels of histone 3 phosphorylation in G1 altering chromatin compaction - and thus more vulnerable to microtubule-driven deformations. The resulting nuclear instability leads to local nuclear reorganisation and changes in 3D genome organisation impacting ultimately gene expression. Importantly, we observed similar nuclear instability in megakaryocytes, which are physiological polyploid cells that we show here to be generated by mitotic slippage, providing a molecular mechanism for their atypical nuclear architecture[6,7]. In striking contrast, nuclear shape was stable in different physiological polyploid cells generated by cytokinesis failure and endoreplication. Overall, our findings highlight that the route towards WGD matters and that mitotic slippage uniquely destabilizes nuclear architecture, with implications for both physiology and disease.

Keywords

Whole Genome Duplication - Polyploidy - Nuclear Architecture - Genome Organization - Mitotic slippage - Nuclear lamins - Histone compaction - H3S10.

Introduction

Most animal cells are diploid, carrying two copies of each chromosome (2N). Through a developmentally regulated and reproducible program, certain cells increase their chromosome number through whole genome duplication (WGD), accumulating multiple sets of each chromosome (> 2N) – hereafter called physiological polyploidy[8]. In most cases, the increase in DNA content is related with an increase in metabolic activity, barrier function or even regenerative capacity. For instance, in mammals, megakaryocytes become polyploid (modal ploidy 16N) to increase their metabolic capacity and produce a high number of platelets[7,9] while salivary gland cells become polyploid (1024N) during *Drosophila* larval development to produce large quantities of glue, which is necessary for *Drosophila* pupation[8,10,11]. Mammalian hepatocytes also become polyploid (8N) during liver maturation. The role of polyploidy in this context is still debated, but previous studies suggested that polyploid hepatocytes may have higher metabolic and regenerative capacities[12,13]. In contrast, when WGD occurs in cells that should not become polyploid - hereafter called unscheduled polyploidy - it leads to genetic and chromosomal instability[2,14–20]. Furthermore, the resulting tetraploidy (4N) - that results from a single WGD - is a common feature of human tumours. Indeed, about 30% of tumours are tetraploid, reaching up to 70% in some specific cases like non-small cell lung carcinomas[4,5,18,21].

The canonical cell cycle typical of somatic cells relies on coupling genome duplication with mitotic cell division to generate two diploid daughter cells[22]. Polyploid cells can be generated by alternative cell cycles - hereafter called non-canonical cell cycles. These cell cycles rely on incomplete or absent mitosis uncoupling the duplication of the genome from cell division leading thus to WGD[1]. Cells can exit mitosis before or after chromosome segregation through mitotic slippage (MS) or cytokinesis failure (CF), respectively (Fig. 1A). Otherwise, cells can alternate S-phase with G-phase using a cell cycle called endoreplication (EnR) (Fig. 1A). MS and EnR generate polyploid cells with a single nucleus, while CF generates binucleated polyploid cells[6,11,23]. However, the functional consequences of these non-canonical cell cycles remain poorly understood. Indeed, while MS, CF and EnR have been proposed to take place in physiological and pathological contexts[1,2,8,12,24], it is still not clear whether different means to reach WGD lead to different outcomes.

Here, by combining comparative analyses integrating physiological and unscheduled models of WGD, we found that MS, unlike CF and EnR, generates polyploid cells with irregular nuclear architecture. Mechanistically, we identified that MS leads to mitotic exit with high levels of histone 3 phosphorylation on serine 10 (H3S10). This impairs chromatin compaction compromising nuclear stiffness and allowing microtubules to promote nuclear deformability. This induces local nuclear reorganisation and changes in 3D genome organization and in gene expression. Importantly, we observed that a similar mechanism contributes to the irregular nuclear shape of megakaryocytes, physiological polyploid cells generated by MS. Overall, these data highlight the fact that different means to generate WGD have different outcomes, which may influence downstream cell functions.

Results

Mitotic slippage, unlike cytokinesis failure and endoreplication, generates tetraploid cells with nuclear deformations

To define whether different routes of WGD have different outcomes, we induced unscheduled WGD through mitotic slippage (MS), cytokinesis failure (CF) or endoreplication (EnR) in RPE-1 cells (see methods, Fig. 1A and Supp. Fig. 1A)[15,25], which are p53-proficient diploid human cell line. As previously described and due to the methods employed to induce WGD[15], this strategy generates a mixed population of diploid (2N) and tetraploid (4N) cells that can be distinguished by nuclear and cell size[15]. Importantly, to avoid any effect due to cell cycle progression, cells were synchronised in the first G1 upon WGD using the CDK4/6 inhibitor Palbociclib[26] at 1μM.

Using these highly comparable systems, we observed that MS, but not CF and EnR, generated tetraploid cells with abnormal nuclear shape (Fig. 1B). To quantitatively analyse the nuclear architecture in these cells, we measured nuclear circularity and solidity, two indices, informing on nuclear elongation and on the presence of nuclear invaginations, respectively (Fig. 1C). We observed that tetraploid cells generated through MS showed decreased nuclear circularity and solidity, while CF and EnR showed values similar to diploid cells (Fig. 1D-F). Similar results were obtained using alternative methods and other diploid cell lines - BJ and HCT116 (Supp. Fig. 1A-H). Additionally, when cells were cultured in 3D, nuclear deformations upon MS were still detected (Supp. Fig. 1I-L). Inducing MS in asynchronous cells, also showed similar results (Supp. Fig. 1M). Interestingly, we found that the nuclear area was similar in MS- and EnR-generated newly born tetraploid cells (Supp. Fig. 1N-O), suggesting that nuclear defects upon MS does not affect the overall nuclear size but only nuclear architecture.

We next performed live imaging approaches using cells stably expressing mCherry-H2B, to follow the transition from G2 to the subsequent G1 at the single cell level. In control diploid cells that undergo canonical mitotic divisions, nuclear circularity and solidity from G2 to G1 remained stable (Fig. 1G-H and Movie 1). In contrast, in tetraploid cells generated by MS an obvious decrease could be noticed (Fig. 1G-H and Movie 2). Plotting the delta circularity (defined as the difference between nuclear

139 circularity in G2 vs in G1) showed values close to 0 in diploid cells (Fig. 1I). This
140 indicates that nuclear architecture was similar before and after mitosis in diploid cells
141 - i.e. nuclear architecture was stable over subsequent cell cycles, as expected. Delta
142 circularity increase in MS-induced tetraploid cells indicates that MS impairs the re-
143 establishment of a typical nuclear architecture in newly born tetraploid cells. Indeed,
144 we observed that MS-induced tetraploid G1 cells exhibited heterogenous nuclear
145 shapes (Fig. 1J), that were still present in the following G2 (Supp Fig. 1P). To
146 understand whether these abnormal shapes were maintained over multiple cell cycles,
147 we induced MS in a p53-depleted RPE-1 cell line, which is permissive to tetraploid cell
148 proliferation[15,27–29]. Nuclear circularity and solidity remained low over multiple cell
149 cycles in MS-generated tetraploid cells (Supp Fig. 1Q-S).
150 At the population level, we were struck by the level of heterogenous nuclear
151 shapes upon MS. Indeed, we found that MS generated a population of tetraploid cells
152 displaying a wide-range of nuclear circularity and solidity indexes (Fig. 1J-K). This
153 reflects that WGD when induced through MS generates a high degree of nuclear shape
154 diversity that seems stochastic - a phenomenon that we called here nuclear instability.
155 In contrast, diploid, CF- and EnR-generated tetraploid cells are clustered in a
156 homogenous cell population with nuclear circularity and solidity indexes close to 1,
157 indicating that these cells have a uniform nuclear architecture (Fig. 1J-K).
158 Together, these findings show that MS generates nuclear instability - i.e. a high
159 degree of nuclear shape diversity, while CF and EnR induction do not impair nuclear
160 morphology.
161
162 **Upon mitotic slippage, cells enter G1 with high H3S10 phosphorylation levels**
163
164 We then investigated why only MS generated nuclear instability. During mitotic entry,
165 phosphorylation of Ser10 of Histone 3 (H3S10) promotes nuclear envelope
166 breakdown[30–32] (Supp. Fig. 2A-B). As cells exited mitosis, the phosphorylation levels
167 gradually decreased allowing nuclear envelope reformation[30,31] (Supp. Fig. 2A-B).
168 Since EnR cells do not enter mitosis, H3S10 phosphorylation levels should remain low
169 throughout the cell cycle, while CF cells exit mitosis in a state in which H3S10
170 phosphorylation levels should also be low[30,31]. In contrast, MS cells, that exit mitosis
171 earlier, should display high H3S10 phosphorylation levels when exiting mitosis[30,31]. In
172 line with this model, we found that MS-induced tetraploid cells still have H3S10

173 phosphorylation in the first G1 upon WGD - forming patches close to the nuclear
174 envelope (Fig. 2A-B). In contrast, diploid or CF-induced tetraploid cells do not exhibit
175 H3S10 phosphorylation in G1 (Fig. 2A-B), as expected[30,31].
176 We next wanted to directly test the contribution of high H3S10 phosphorylation
177 levels to nuclear architecture. We generated a cell line, expressing an H3 mutant
178 version, where Serine 10 was replaced by an Alanine residue - H3S10A[30], in the
179 background of wild type (WT) H3. A partial decrease in H3S10 phosphorylation during
180 mitosis was noticed as expected (Supp. Fig. 2C). Importantly, this was sufficient to
181 increase both nuclear circularity and solidity in newly born tetraploid MS-induced cells,
182 improving their overall nuclear shape and thus decreasing nuclear instability (Fig. 2C-
183 D and Supp. Fig 2D-E). To confirm that maintaining H3S10 phosphorylation in G1 was
184 sufficient to generate nuclear deformations, we inhibited the phosphatase responsible
185 for H3S10 dephosphorylation at mitotic exit using Calyculin A[33] in diploid cells. This
186 treatment resulted in increased H3S10 phosphorylation levels in diploid G1 cells and
187 remarkably, nuclear deformations characterized by invaginations similar to those found
188 in MS-generated tetraploid cells were noticed (Supp. Fig. 2F-G).
189 Together, our results show that low H3S10 phosphorylation at mitotic exit is a
190 pre-requisite to re-establish proper nuclear morphology during nuclear re-assembly.
191
192 **Mitotic slippage generates tetraploid cells with high histone acetylation levels**
193 **and low nuclear stiffness**
194
195 We then investigated the mechanism underlying nuclear deformations upon MS.
196 Previous work identified that H3S10 phosphorylation impacts other histone
197 modifications[34–37]. We thus quantified histone acetylation and methylation levels using
198 structural illumination microscopy. The fluorescence intensity levels were measured in
199 diploid and tetraploid G1 cells at the level of the whole nucleus (Supp. Fig. 3A).
200 We first noticed a global increase in H3K9ac, H3K27ac and H3K14ac levels in
201 tetraploid G1 cells generated by MS (Fig. 2E-G and Supp. Fig. 3B). In contrast, in CF-
202 or EnR-induced tetraploid G1 cells, histone acetylation remained similar to diploid cells
203 (Fig. 2F-G and Supp. Fig. 3B). Importantly, reducing H3S10 phosphorylation by
204 expressing H3S10A mutant was sufficient to prevent the increase in acetylation levels
205 observed upon MS (Supp. Fig. 3C). This suggests that high H3S10 phosphorylation
206 levels upon MS induced a global increase in histone acetylation in tetraploid G1 cells.

207 Since histone acetylation is commonly associated with open chromatin/euchromatin[38],
208 we performed ATACseq and found that chromatin accessibility was higher in MS-
209 induced tetraploid G1 cells compared to diploid cells (Fig. 2H).

210 When measuring histone methylation, usually associated with closed
211 chromatin/heterochromatin[39,40], we found that only H3K9me2 levels were increased
212 upon MS, while H3K9me3 and H3K27me3 levels remained similar to diploid cells
213 (Supp. Fig 3D-F). In CF- or EnR-generated cells, no changes in histone methylation
214 levels were found (Supp. Fig. 3G-H). Interestingly, we also observed that MS led to a
215 decrease in the number of Heterochromatin Protein 1α (HP1α) foci (Supp. Fig. 3I-J), a
216 key component known to promote nuclear compaction[41]. Together, these findings
217 demonstrate that MS impairs histone compaction in newly born tetraploid cells
218 favouring an overall open chromatin.

219 It is well established that several factors, including chromatin states, contribute
220 to nuclear envelope deformability counteracting cytoplasmic forces that act on the
221 nucleus[42,43]. It is therefore possible that the nuclear deformations of tetraploid cells
222 induced through MS reflected a decrease in nuclear mechanical properties due to
223 changes in chromatin compaction as described above. To test this possibility, we first
224 tested whether MS alters nuclear stiffness using atomic force microscopy (AFM) (Fig
225 2I). Using two different strategies to generate MS, we found that G1 tetraploid nuclei
226 were significantly softer than their diploid counterparts (Fig. 2J and Supp. Fig. 3K). In
227 contrast, CF-induced tetraploid G1 cells exhibit nuclear stiffness similar to diploid cells
228 (Fig. 2J).

229 We next investigated the functional relationship between higher acetylation
230 levels, decreased nuclear stiffness and nuclear deformations upon MS. We used two
231 complementary strategies to decrease acetylation levels in MS-induced tetraploid
232 cells. We treated cells with (1) C646, a histone acetylase inhibitor[44], which decreases
233 histone acetylation levels (Supp. Fig. 4A) or with (2) Methylstat, a histone demethylase
234 inhibitor[45], which promotes histone methylation preventing histone acetylation on the
235 same residues (Supp. Fig. 4A-B). These treatments were sufficient to decrease histone
236 acetylation and to promote nuclear compaction and thus nuclear stiffness preventing
237 nuclear deformations and nuclear instability in MS-induced tetraploid G1 cells (Fig. 2K-
238 N and Supp. Fig. 4A-F). These results were confirmed using JIB, another histone
239 demethylase inhibitor[46], by live imaging, using another method to induce MS and in BJ
240 and HCT116 cells (Supp. Fig. 4G-O).

241 These data show that MS generates tetraploid cells with high levels of chromatin
242 acetylation that contribute to decrease their nuclear stiffness.
243
244 **Microtubules generate nuclear invaginations in MS-induced tetraploid G1 cells**
245
246 Detailed analysis of mitotic exit in diploid and MS-induced tetraploid cells revealed an
247 increase in nuclear area, most likely due to chromosome decondensation[47]. However,
248 in tetraploid cells, this was accompanied by the appearance of nuclear invaginations
249 (Supp. Fig 5A, pink arrow). Indeed, while quantifying nuclear circularity and solidity,
250 we found that these indices were quite stable in diploid cells during early G1 (Supp.
251 Fig 5B, upper panel), whereas both parameters decreased in newly born tetraploid
252 cells during mitotic exit (Supp. Fig 5B, lower panel).
253 Cytoskeleton components interact with the nuclear envelope, a process that
254 contributes to the establishment of nuclear architecture[48]. Using time-lapse microscopy
255 in cells incubated with SPY-Tubulin and SPY-Actin, we followed microtubules and
256 actin, respectively. Characterization of cytoskeleton proteins in G1 cells showed that
257 microtubules (but not actin) accumulated at nuclear invaginations in MS-induced
258 tetraploid cells (Supp. Fig 5C-E), which was not seen in EnR-generated tetraploid cells
259 (Supp. Fig. 5F). We found that just after nuclear envelope reformation upon MS,
260 microtubules accumulated at invagination sites assembling in thick bundles whereas
261 actin did not (Supp. Fig. 5G-H and Movies 3-4). These data suggest that microtubules
262 unlike actin, contribute to nuclear instability in newly born tetraploid cells.
263 To functionally test the contribution of microtubules in generating nuclear
264 invaginations, we removed microtubules using nocodazole, a microtubule-
265 depolymerizing agent[49], just before MS (Supp. Fig. 6A-B and Movie 5-6). Strikingly, in
266 the absence of microtubules, the nuclear shape in newly born tetraploid cells became
267 more regular, presenting fewer deformations in G1, as also revealed by a decrease in
268 the delta circularity (Supp. Fig. 6B). Moreover, treating tetraploid cells with nocodazole
269 was sufficient to enhance both nuclear circularity and solidity reducing thus nuclear
270 instability (Supp. Fig. 6C-D). These results were confirmed using another mean to
271 induce MS (Supp. Fig. 6E-G and Movie 7-8). We then tested whether stabilizing
272 microtubules could exacerbate nuclear deformations. To do so, we treated tetraploid
273 cells with low-doses of Taxol, a microtubule-stabilizing agent[50], before MS. In these
274 conditions, nuclear deformations were even more impressive and a decrease in both

275 nuclear circularity and solidity was noticed associated with a higher nuclear instability
276 (Supp. Fig. 6H-I).
277 We conclude that the microtubule cytoskeleton is the main contributor to nuclear
278 deformations in newly born tetraploid cells induced by unscheduled MS.
279
280 **Nuclear deformations upon mitotic slippage leads to local nuclear**
281 **reorganisation**
282
283 We then investigated whether the nuclear deformations upon MS have a local impact
284 on nuclear architecture. To do so, we conducted a mini screen in which 8 chromatin-
285 related and 6 nuclear envelope-related candidates were visually examined using
286 structural illumination microscopy. The candidate list was compiled based on their well-
287 established roles in nuclear morphology[30,42,43,51–54] and the fluorescence intensity
288 levels were measured in diploid and tetraploid G1 cells at intact and deformed nuclear
289 envelope regions.
290 This mini screen identified that H3K9me2 levels were decreased in specific
291 regions that coincide with nuclear deformations in MS-induced tetraploid cells (Fig. 3A-
292 D). Because the tools used to characterize H3K9me2 are the subject of controversial
293 studies[55], we also used another H3K9me2 antibody and two different protocols and
294 observed the same results (Supp. Fig. 7A-C). H3K9me2 is normally enriched at the
295 nuclear periphery and associated with chromatin regions that are less dynamic[30,54].
296 H3K9me2 coefficient of variation (CoV) at the nuclear envelope (defined as the ratio
297 of the standard deviation to the mean) was increased in tetraploid cells generated by
298 MS (Supp. Fig. 7D), indicating uneven distribution of this modification, in sharp contrast
299 with the uniform distribution of H3K9me2 at the nuclear envelope of diploid nuclei (Fig.
300 3D and Supp. Fig. 7D). Similar defects in H3K9me2 localization at invaginations were
301 found in tetraploid cells where MS was induced by a different mean, and in BJ and
302 HCT116 cell lines (Supp. Fig. 7E-G). In contrast, we observed that both CF- and EnR-
303 induced tetraploid cells displayed homogeneous distributions of H3K9me2 (Fig. 3A-C
304 and Supp. Fig. 7H-I). Moreover, no local changes in H3K9me3, H3K27me3, H3K9ac
305 and H3K27ac levels, were noticed upon MS (Supp. Fig. 7J-K).
306 The Lamina, composed of a specific ratio of Lamin A/C and Lamin B proteins,
307 plays a crucial role in maintaining nuclear architecture[43,51,52,56,57]. The ratio between
308 Lamin A/C and B is crucial in establishing nuclear morphology[51,52,56,57]. Indeed, nuclear

309 resistance is strongly impacted by Lamin A/C and a ratio dominated by Lamin B has
310 thus been associated with soft tissues[56,57]. By measuring this ratio, we found
311 differences in tetraploid cells at nuclear deformations regions. Frequently, Lamin B1
312 dominated the lamina network in invaginated domains, while the levels of Lamin A/C
313 were lower than the ones found in intact regions (Fig. 3A-D). In line with this, we found
314 that Lamin B Receptor (LBR) levels - a protein associated with soft tissues[58] - were
315 also increased locally at the nuclear deformations upon MS, while we found no
316 changes in Lap2β, Emerin and Nuclear pore complex levels (Supp Fig. 7L). Similar
317 defects were observed in MS-generated tetraploid cells using an alternative method
318 and in BJ and in HCT116 cell lines (Supp. Fig. 7E-G). In contrast, we observed that
319 both EnR- and CF-induced tetraploid cells displayed homogeneous Lamin ratios (Fig.
320 3A-C and Supp. Fig. 7H). Importantly, preventing nuclear deformations upon MS by
321 reducing histone acetylation or by depolymerizing microtubules was sufficient to
322 restore homogeneous distributions of H3K9me2 and Lamin ratios in tetraploid cells
323 (Fig. 3E and Supp. Fig. 7M).
324 Together, our findings show that nuclear deformations upon MS promote local
325 changes in nuclear organisation.
326
327 **Mitotic slippage impairs 3D genome organisation and gene expression**
328
329 We next investigated the functional consequences of nuclear deformations observed
330 upon MS. Recently it has been shown that WGD in p53-deficient cells leads to loss of
331 chromatin segregation explained by an increased proportion of contacts between
332 chromosomes, compartments, and chromatin domains[59]. Insulation of topology
333 associated domains (TADs) requires a certain number of proteins that do not seem to
334 scale with the tetraploid genome[59]. We wanted to investigate whether such defects
335 were already detectable in the first G1 after MS, in the presence of p53. To do so, we
336 isolated diploid and tetraploid cells using flow cytometry, as previously described[15]
337 (Supp. Fig. 8A-B). Importantly, cell sorting did not affect nuclear deformations in MS-
338 generated tetraploid cells (Supp. Fig. 8C). Using high throughput chromatin capture
339 conformation (HiC), we compared interactions at the chromosomal level and between
340 chromatin domains in diploid and newly born MS-generated tetraploid G1 cells.
341 Similarly to what has been previously observed, we found an increased number of

342 contacts between short and long chromosomes (Fig. 3H) and between A and B
343 compartments (Supp. Fig. 8D-G) in tetraploid cells compared to diploid cells.
344 Our findings showing changes in genome organisation and chromatin state /
345 accessibility upon MS led us to test whether MS alters gene expression. We thus
346 analysed newly born tetraploid cells in the first G1 upon MS by RNAseq. We found that
347 150 genes were deregulated in tetraploid G1 cells compare to diploid G1 cells (Supp.
348 Fig. 8H).
349 Overall, our results identified that MS perturbs 3D genome organisation in newly
350 born tetraploid cells culminating with changes in gene expression.
351
352 **Megakaryocytes undergo mitotic slippage and display nuclear instability**
353
354 We decided to determine whether physiological polyploid cells generated by MS also
355 exhibit nuclear deformations. To do so, we analysed megakaryocytes, differentiated
356 polyploid cells, derived from hematopoietic progenitors[7], and responsible for
357 production of RNAs and proteins that will be transported to the cell tips to generate
358 anucleate platelets[9]. To obtain megakaryocytes, we isolated mouse diploid
359 hematopoietic stem cells and induced their differentiation *in vitro* using a cocktail of
360 cytokines (Fig. 4A). We obtained a population of primary cells composed of diploid
361 hematopoietic stem cells / progenitors and polyploid megakaryocytes showing different
362 cell and nuclear sizes. These differences in size reflect a ploidy continuum and allow
363 us to identify polyploid cells (Supp. Fig. 9A-B). Using live imaging approaches of
364 megakaryocytes isolated from mice expressing H2B-mCherry, we observed that nuclei
365 exit mitosis without chromosome segregation or following limited movement during
366 anaphase A. These lack any sign of cytokinesis furrowing confirming MS (Fig. 4B and
367 Movie 9-10), as previously suggested[7,60].
368 In our hands, and in agreement with *in vivo* analysis[6,7], megakaryocytes
369 displayed a single multilobulated highly deformed nucleus (Fig. 4C). Quantification of
370 circularity and solidity revealed a decrease in a ploidy-dependent manner (Fig. 4D-F).
371 Similarly to MS-induced RPE-1 cells, we observed that megakaryocyte nuclear shapes
372 were highly heterogenous (Fig 4G-H). This reflects that megakaryocyte
373 polyploidization by MS also generates nuclear instability. When comparing with other
374 physiological polyploid cells, we noticed that nuclear instability was specific to
375 megakaryocytes. Indeed, analysis of polyploid hepatocytes isolated from mouse liver,

376 that become polyploid by CF[12,13] or *Drosophila* salivary glands, that become polyploid
377 by EnR[8,10], showed homogeneous circular nuclei lacking nuclear deformations (Fig
378 4D-H and Supp. Fig. 9C-I). Similar observations were made *in vivo* in two other
379 polyploid *Drosophila* tissues – the fat body and the ring gland that become polyploid
380 by EnR[3] (Supp. Fig. 9J).
381 Together, these findings show that MS, but not CF or EnR impact nuclear shape
382 and stability in physiological polyploid settings.
383
384 **Mitotic slippage in megakaryocytes is associated with changes in chromatin**
385 **compaction and nuclear envelope composition**
386
387 Our results in RPE-1 cells show that MS-induced tetraploid cells exhibit changes in
388 chromatin compaction and nuclear envelope composition promoting nuclear softness
389 and deformability facilitating nuclear deformations by the microtubules. We therefore
390 considered the possibility that megakaryocytes undergo a similar process.
391 We first tested whether histone compaction was altered upon MS in
392 megakaryocytes. We found an increase in H3K27ac and H3K9ac levels in small
393 megakaryocytes (Fig. 5A-B) while H3K14ac levels were increased in both small and
394 large megakaryocytes (Supp. Fig. 10A). We also observed a global decrease in
395 H3K9me2 levels with megakaryocyte ploidy while H3K9me3 levels remained
396 comparable between progenitors and megakaryocytes (Supp. Fig. 10B-C).
397 Interestingly, a local decrease in H3K9me2 levels in deformed regions was also found
398 in megakaryocytes using two different antibodies (Supp. Fig. 10E-H). Concerning the
399 nuclear envelope composition, a striking switch in Lamina composition during
400 megakaryocyte differentiation was observed. Small and large megakaryocytes
401 displayed lower levels of Lamin A/C than diploid progenitors, while Lamin B1 levels
402 remained largely unchanged (Fig. 5C-D and Supp. Fig. 10D). In contrast, defects in
403 H3K9me2 distribution and Lamina composition in hepatocytes or in the Lamina
404 network in salivary gland cells were not detected (Supp. Fig. 10J-R). The high levels
405 of histone acetylation and the decrease in Lamin A/C levels in megakaryocytes – two
406 phenotypes associated with softer nuclei[43] - are consistent with previous data showing
407 that nuclear stiffness decreased during megakaryocyte differentiation[61]. To confirm
408 that low nuclear stiffness contributes to nuclear deformations in megakaryocytes we
409 promoted nuclear compaction by treating cells with Methylstat using a similar strategy

410 as described above for RPE-1 cells. This was sufficient to alter nuclear shape and to
411 reduce nuclear instability in megakaryocytes (Fig. 5E-G). Together, these findings
412 suggest that during differentiation, megakaryocytes are in a state in which nuclear
413 resistance is low - due to changes in chromatin compaction and nuclear envelope
414 composition - favouring nuclear deformability. We next investigated whether the
415 microtubule cytoskeleton also contribute to the nuclear deformations in
416 megakaryocytes. We found thick microtubule bundles positioned around nuclear
417 invaginations (Supp. Fig. 10I), which were absent in hepatocytes or salivary glands. In
418 these former examples, the microtubule cytoskeleton was organized around the
419 nucleus forming a microtubule ring (Supp. Fig. 10S). Importantly, removing
420 microtubules was sufficient to decrease the nuclear instability in megakaryocytes
421 (Supp. Fig. 10T), similarly to what was observed in RPE-1 MS-induced tetraploid cells.
422 These results suggest that highly specialized and differentiated cells such as
423 polyploid megakaryocytes rely on low nuclear stiffness to generate cells with irregular
424 nuclear architecture *in vivo*. Importantly, our findings also identified the molecular
425 mechanism underlying the irregular nuclear shape in megakaryocytes, initially
426 described 50 years ago[6].

427 ## Discussion

428

429 In this study, we show that different routes to WGD lead to different outcomes. Indeed,
430 MS, unlike CF and EnR, generated tetraploid cells displaying abnormal nuclear
431 configurations. These defects include maintenance of high H3S10 phosphorylation
432 levels in G1, which seem to promote histone acetylation and thus decreased nuclear
433 stiffness. Due to the increased nuclear deformability, cytoplasmic microtubules
434 generate nuclear invaginations that coincide with local changes in the chromatin /
435 nuclear envelope composition. These findings are supported by other studies, which
436 have shown that microtubules, Lamins and peripheral heterochromatin also contribute
437 to nuclear morphology in diploid cells[42,62–64]. Together, these defects produce a
438 heterogenous population of polyploid nuclei with various shapes - that we defined as
439 nuclear instability - culminating with changes in 3D genome organisation as well as in
440 gene expression (Fig. 5H).

441 Importantly, we observed these defects in the first G1 upon MS contributing to a
442 better understanding of the early consequences of WGD. However, while the extent of
443 the nuclear deformations is visually impressive, the effects on 3D genome organisation
444 and on gene expression remain mild, even if significant, in the first G1 upon MS. This
445 suggest that tetraploid cells can, at least in part, deal with these defects. Nevertheless,
446 we cannot exclude that these early changes may be amplified after subsequent cell
447 cycles.

448 MS, CF and EnR have been proposed to be at the origin of WGD in tumours[2,12,24],
449 but little is known about their proportion and respective role in cancer. Nuclear
450 deformations were observed in tumours since the mid-nineteenth century and are even
451 used for diagnostic in some situations[65], but a potential link with WGD and MS was
452 never established. It remains to be understood whether nuclear deformations and
453 instability, typical of MS, contribute to the tumorigenic process. MS, CF and EnR are
454 also involved in developmental programs generating physiological polyploid
455 cells[7,8,13,66]. Whether these different strategies reflect a particular advantage or are just
456 byproducts of selective pressure remains unknown.

457 Interestingly, to our knowledge, megakaryocytes are the only example of MS-
458 generated physiological polyploid cells, making them quite unique. By showing that
459 megakaryocytes display changes in chromatin / nuclear envelope composition that
460 contributes to nuclear deformations, we exposed a molecular mechanism underlying

461 the generation of megakaryocytes with irregular nuclear architecture. It has been
462 shown that megakaryocyte reprogramming to induce polyploidy through EnR instead
463 of MS contributes to prevent nuclear deformations[60], confirming the predominant role
464 of MS in generating megakaryocytes with irregular architecture. The global changes in
465 chromatin state that we observed upon MS may contribute to alterations in gene
466 expression sustaining the required transcriptomic changes described during
467 megakaryocyte differentiation[67].

468 Overall, our findings show that the cell cycle route chosen to generate polyploid
469 cells has different outcomes. More importantly, our results highlight the fact that in
470 physiological and pathological conditions, different methods to induce WGD have the
471 potential to generate polyploid cells with specific features contributing to their inherent
472 function.

Acknowledgments

The authors acknowledge the Cell and Tissue Imaging (PICT-IBiSA) from Institut Curie, member of the national infrastructure France-BioImaging (https://ror.org/01y7vt929) supported by the French National Research Agency (ANR-24-INBS-0005 FBI BIOGEN) and V. Fraisier, C. Guedj. M. David, M. Cortes and A.S. Macé (PICT-IBiSA) for their continuous support on image acquisition and analysis. We thank L. Guyonnet, A. Chipont, A.G. Lafont and C. Guerrin from the Cytometry platform of Institut Curie. High-throughput sequencing was performed by the ICGex NGS platform of the Institut Curie supported by the grants ANR-10-EQPX-03 (Equipex) and ANR-10-INBS-09-08 (France Génomique Consortium) from the Agence Nationale de la Recherche ("Investissements d'Avenir" program), by the ITMO-Cancer Aviesan (Plan Cancer III) and by the SiRIC-Curie program (SiRIC Grant INCa-DGOS-465 and INCa-DGOS-Inserm_12554). Data management, quality control and primary analysis were performed by the Bioinformatics platform of the Institut Curie. We thank Genosplice (http://www.genosplice.com) and more specifically P. Delagrange and M. Caron for RNAseq and ATACseq analysis and for their valuable work. We thank A. Rodriguez-Romera and B. Psaila for sharing unpublished work. We thank A. Poleshko and JA Epstein for sharing the plasmids expressing H3WT and H3S10A. We thank A. Donada, J. Cossgrove and L. Perie, for teaching us the secrets of megakaryocyte differentiation and together with M. Piel and U. Kutay for helpful discussions and/or comments on the manuscript. GA's team has been supported by the European Research Council (ERC-2015-ADG-694694 ChromADICT), the Ligue Nationale contre le Cancer (Equipe labellisée Ligue), France and Agence Nationale de la Recherche, France (ANR-11-LABX-0044_DEEP, ANR-10-IDEX-0001-02 PSL). N.W has been supported by the FRM. This work has been funded by InCA (www.e-cancer.fr) (2021-1- PREV-Bio grant), the government through the Agence Nationale de la Recherche from France 2030 (ANR-23-CHBS-0012), the Institut Curie and the CNRS.

Author's contribution

S.G. and R.B. conceived the project. S.G. wrote the manuscript. S.G. and M.B. did most of the experiments and data analysis presented here. S.A., F.SdC., C.V. and V.M. contributed to the HSC purification. A.S. prepared the RNA used for the RNAseq. Y.M. and S.W. performed the AFM with the help of S.G. and M.B. J.F. and C.D. contributed by isolating the mouse hepatocytes. R.L., G.C. and E.O. performed the

HiC experiments. N.W, A.F. and G.A. designed and performed the ATACseq experiments with the help of S.G. and M.B. R.B. obtained the funding used to develop this project. All authors read and commented on the manuscript.

Declaration of interests

The authors declare no competing interests.

References

1. Gemble, S. & Basto, R. CHRONOCRISIS: When Cell Cycle Asynchrony Generates DNA Damage in Polyploid Cells. *BioEssays News Rev. Mol. Cell. Dev. Biol.* **42**, e2000105 (2020).
2. Ganem, N. J., Storchova, Z. & Pellman, D. Tetraploidy, aneuploidy and cancer. *Curr. Opin. Genet. Dev.* **17**, 157–162 (2007).
3. Orr-Weaver, T. L. When bigger is better: the role of polyploidy in organogenesis. *Trends Genet.* **31**, 307–315 (2015).
4. Bielski, C. M. *et al.* Genome doubling shapes the evolution and prognosis of advanced cancers. *Nat. Genet.* **50**, 1189–1195 (2018).
5. Zack, T. I. *et al.* Pan-cancer patterns of somatic copy number alteration. *Nat. Genet.* **45**, 1134–1140 (2013).
6. Penington, D. G. & Streatfield, K. Heterogeneity of megakaryocytes and platelets. *Ser. Haematol. 1968* **8**, 22–48 (1975).
7. Mazzi, S., Lordier, L., Debili, N., Raslova, H. & Vainchenker, W. Megakaryocyte and polyploidization. *Exp. Hematol.* **57**, 1–13 (2018).
8. Frawley, L. E. & Orr-Weaver, T. L. Polyploidy. *Curr. Biol. CB* **25**, R353-358 (2015).
9. Carminita, E., Becker, I. C. & Italiano, J. E. What It Takes To Be a Platelet: Evolving Concepts in Platelet Production. *Circ. Res.* **135**, 540–549 (2024).
10. Zielke, N. *et al.* Control of Drosophila endocycles by E2F and CRL4(CDT2). *Nature* **480**, 123–127 (2011).
11. Sigrist, S. J. & Lehner, C. F. Drosophila fizzy-related down-regulates mitotic cyclins and is required for cell proliferation arrest and entry into endocycles. *Cell* **90**, 671–681 (1997).
12. Davoli, T. & de Lange, T. The causes and consequences of polyploidy in normal development and cancer. *Annu. Rev. Cell Dev. Biol.* **27**, 585–610 (2011).
13. Gentric, G. & Desdouets, C. Liver polyploidy: Dr Jekyll or Mr Hide? *Oncotarget* **6**, 8430–8431 (2015).
14. Nano, M. *et al.* Cell-Cycle Asynchrony Generates DNA Damage at Mitotic Entry in Polyploid Cells. *Curr. Biol.* **29**, 3937-3945.e7 (2019).
15. Gemble, S. *et al.* Genetic instability from a single S phase after whole-genome duplication. *Nature* **604**, 146–151 (2022).
16. Kirsch-Volders, M., Mišík, M. & Fenech, M. Tetraploidy in normal tissues and diseases: mechanisms and consequences. *Chromosoma* **134**, 3 (2025).
17. Goupil, A. *et al.* Chromosomes function as a barrier to mitotic spindle bipolarity in polyploid cells. *J. Cell Biol.* **219**, e201908006 (2020).
18. López, S. *et al.* Interplay between whole-genome doubling and the accumulation of deleterious alterations in cancer evolution. *Nat. Genet.* **52**, 283–293 (2020).
19. Prasad, K. *et al.* Whole-Genome Duplication Shapes the Aneuploidy Landscape of Human Cancers. *Cancer Res.* **82**, 1736–1752 (2022).
20. Kuznetsova, A. Y. *et al.* Chromosomal instability, tolerance of mitotic errors and multidrug resistance are promoted by tetraploidization in human cells. *Cell Cycle Georget. Tex* **14**, 2810–2820 (2015).
21. Blakely, C. M. *et al.* Evolution and clinical impact of co-occurring genetic alterations in advanced-stage EGFR-mutant lung cancers. *Nat. Genet.* **49**, 1693–1704 (2017).
22. Basu, S., Greenwood, J., Jones, A. W. & Nurse, P. Core control principles of the eukaryotic cell cycle. *Nature* **607**, 381–386 (2022).
23. Guidotti, J.-E. *et al.* Liver cell polyploidization: a pivotal role for binuclear hepatocytes. *J. Biol. Chem.* **278**, 19095–19101 (2003).

24. Zeng, J., Hills, S. A., Ozono, E. & Diffley, J. F. X. Cyclin E-induced replicative stress drives p53-dependent whole-genome duplication. *Cell* **186**, 528-542.e14 (2023).
25. Bernhard, S. V., Gemble, S., Basto, R. & Storchova, Z. Experimental Approaches to Generate and Isolate Human Tetraploid Cells. *Methods Mol. Biol. Clifton NJ* **2545**, 391–399 (2023).
26. Fry, D. W. *et al.* Specific inhibition of cyclin-dependent kinase 4/6 by PD 0332991 and associated antitumor activity in human tumor xenografts. *Mol. Cancer Ther.* **3**, 1427–1438 (2004).
27. Ganem, N. J. *et al.* Cytokinesis Failure Triggers Hippo Tumor Suppressor Pathway Activation. *Cell* **158**, 833–848 (2014).
28. Vittoria, M. A. *et al.* A genome-wide microRNA screen identifies regulators of tetraploid cell proliferation. *Mol. Biol. Cell* **29**, 1682–1692 (2018).
29. Kuffer, C., Kuznetsova, A. Y. & Storchová, Z. Abnormal mitosis triggers p53-dependent cell cycle arrest in human tetraploid cells. *Chromosoma* **122**, 305–318 (2013).
30. Poleshko, A. *et al.* H3K9me2 orchestrates inheritance of spatial positioning of peripheral heterochromatin through mitosis. *eLife* **8**, e49278 (2019).
31. Prigent, C. & Dimitrov, S. Phosphorylation of serine 10 in histone H3, what for? *J. Cell Sci.* **116**, 3677–3685 (2003).
32. Hendzel, M. J. *et al.* Mitosis-specific phosphorylation of histone H3 initiates primarily within pericentromeric heterochromatin during G2 and spreads in an ordered fashion coincident with mitotic chromosome condensation. *Chromosoma* **106**, 348–360 (1997).
33. Ishihara, H. *et al.* Calyculin A and okadaic acid: inhibitors of protein phosphatase activity. *Biochem. Biophys. Res. Commun.* **159**, 871–877 (1989).
34. Chen, C. C. L. *et al.* H3S10ph broadly marks early-replicating domains in interphase ESCs and shows reciprocal antagonism with H3K9me2. *Genome Res.* **28**, 37–51 (2018).
35. Peng, Q. *et al.* Coordinated histone modifications and chromatin reorganization in a single cell revealed by FRET biosensors. *Proc. Natl. Acad. Sci. U. S. A.* **115**, E11681–E11690 (2018).
36. Komar, D. & Juszczynski, P. Rebelled epigenome: histone H3S10 phosphorylation and H3S10 kinases in cancer biology and therapy. *Clin. Epigenetics* **12**, 147 (2020).
37. Mateescu, B., England, P., Halgand, F., Yaniv, M. & Muchardt, C. Tethering of HP1 proteins to chromatin is relieved by phosphoacetylation of histone H3. *EMBO Rep.* **5**, 490–496 (2004).
38. Chen, Y.-J. C., Koutelou, E. & Dent, S. Y. R. Now open: Evolving insights to the roles of lysine acetylation in chromatin organization and function. *Mol. Cell* **82**, 716–727 (2022).
39. Maison, C. & Almouzni, G. HP1 and the dynamics of heterochromatin maintenance. *Nat. Rev. Mol. Cell Biol.* **5**, 296–304 (2004).
40. James, T. C. *et al.* Distribution patterns of HP1, a heterochromatin-associated nonhistone chromosomal protein of Drosophila. *Eur. J. Cell Biol.* **50**, 170–180 (1989).
41. Allshire, R. C. & Madhani, H. D. Ten principles of heterochromatin formation and function. *Nat. Rev. Mol. Cell Biol.* **19**, 229–244 (2018).
42. Stephens, A. D., Banigan, E. J. & Marko, J. F. Chromatin's physical properties shape the nucleus and its functions. *Curr. Opin. Cell Biol.* **58**, 76–84 (2019).
43. Miroshnikova, Y. A. & Wickström, S. A. Mechanical Forces in Nuclear Organization. *Cold Spring Harb. Perspect. Biol.* **14**, a039685 (2022).
44. Bowers, E. M. *et al.* Virtual ligand screening of the p300/CBP histone acetyltransferase: identification of a selective small molecule inhibitor. *Chem. Biol.* **17**, 471–482 (2010).
45. Stephens, A. D. *et al.* Chromatin histone modifications and rigidity affect nuclear morphology independent of lamins. *Mol. Biol. Cell* **29**, 220–233 (2018).

46. Wang, L. *et al.* A small molecule modulates Jumonji histone demethylase activity and selectively inhibits cancer growth. *Nat. Commun.* **4**, 2035 (2013).
47. Moreno-Andrés, D., Holl, K. & Antonin, W. The second half of mitosis and its implications in cancer biology. *Semin. Cancer Biol.* **88**, 1–17 (2023).
48. Rothballer, A. & Kutay, U. The diverse functional LINCs of the nuclear envelope to the cytoskeleton and chromatin. *Chromosoma* **122**, 415–429 (2013).
49. De Brabander, M., De May, J., Joniau, M. & Geuens, G. Ultrastructural immunocytochemical distribution of tubulin in cultured cells treated with microtubule inhibitors. *Cell Biol. Int. Rep.* **1**, 177–183 (1977).
50. Manfredi, J. J. & Horwitz, S. B. Taxol: an antimitotic agent with a new mechanism of action. *Pharmacol. Ther.* **25**, 83–125 (1984).
51. Dechat, T., Adam, S. A., Taimen, P., Shimi, T. & Goldman, R. D. Nuclear lamins. *Cold Spring Harb. Perspect. Biol.* **2**, a000547 (2010).
52. Lammerding, J. *et al.* Lamins A and C but not lamin B1 regulate nuclear mechanics. *J. Biol. Chem.* **281**, 25768–25780 (2006).
53. Janin, A., Bauer, D., Ratti, F., Millat, G. & Méjat, A. Nuclear envelopathies: a complex LINC between nuclear envelope and pathology. *Orphanet J. Rare Dis.* **12**, 147 (2017).
54. Delaney, K., Weiss, N. & Almouzni, G. The cell-cycle choreography of H3 variants shapes the genome. *Mol. Cell* **83**, 3773–3786 (2023).
55. Chudzik, K. *et al.* Ab-trapping - a peripheral staining artifact in antibody-based microscopy and genomics. 2025.04.09.648027 Preprint at https://doi.org/10.1101/2025.04.09.648027 (2025).
56. Ovsiannikova, N. L. *et al.* Lamin A as a Determinant of Mechanical Properties of the Cell Nucleus in Health and Disease. *Biochem. Biokhimiia* **86**, 1288–1300 (2021).
57. Swift, J. *et al.* Nuclear lamin-A scales with tissue stiffness and enhances matrix-directed differentiation. *Science* **341**, 1240104 (2013).
58. Buxboim, A. *et al.* Coordinated increase of nuclear tension and lamin-A with matrix stiffness outcompetes lamin-B receptor that favors soft tissue phenotypes. *Mol. Biol. Cell* **28**, 3333–3348 (2017).
59. Lambuta, R. A. *et al.* Whole-genome doubling drives oncogenic loss of chromatin segregation. *Nature* **615**, 925–933 (2023).
60. Trakala, M. *et al.* Functional reprogramming of polyploidization in megakaryocytes. *Dev. Cell* **32**, 155–167 (2015).
61. Shin, J.-W. *et al.* Lamins regulate cell trafficking and lineage maturation of adult human hematopoietic cells. *Proc. Natl. Acad. Sci. U. S. A.* **110**, 18892–18897 (2013).
62. Biedzinski, S. *et al.* Microtubules control nuclear shape and gene expression during early stages of hematopoietic differentiation. *EMBO J.* **39**, e103957 (2020).
63. Tariq, Z. *et al.* Lamin A and microtubules collaborate to maintain nuclear morphology. *Nucl. Austin Tex* **8**, 433–446 (2017).
64. Nava, M. M. *et al.* Heterochromatin-Driven Nuclear Softening Protects the Genome against Mechanical Stress-Induced Damage. *Cell* **181**, 800-817.e22 (2020).
65. de Las Heras, J. I. & Schirmer, E. C. The nuclear envelope and cancer: a diagnostic perspective and historical overview. *Adv. Exp. Med. Biol.* **773**, 5–26 (2014).
66. Girdler, G. C. & Röper, K. Controlling cell shape changes during salivary gland tube formation in Drosophila. *Semin. Cell Dev. Biol.* **31**, 74–81 (2014).
67. De Wispelaere, K. & Freson, K. The Analysis of the Human Megakaryocyte and Platelet Coding Transcriptome in Healthy and Diseased Subjects. *Int. J. Mol. Sci.* **23**, 7647 (2022).

660 **METHODS**

661

662 **Human cell culture and generation of cell lines:**

663 - *Cell culture:*

664 Cells were maintained at 37°C in a 5% CO_2 atmosphere. hTERT RPE-1 cells (female, ATCC
665 Cat# CRL-4000, RRID:CVCL_4388), HEK293T cells (female, ATCC Cat# CRL-1573,
666 RRID:CVCL_0045), BJ cells (male, ATCC Cat# CRL-4001, RRID:CVCL_6573) and HCT116
667 cells (male, ATCC Cat# CCL-247, RRID:CVCL_0291) were grown in Dulbecco's modified
668 medium (DMEM) F12 (11320-033 from Gibco) containing 10% fetal bovine serum (GE
669 Healthcare), 100 U/ml penicillin, 100 U/ml streptomycin (15140-122 from Gibco).

670

671 All cells were routinely checked and tested negative for mycoplasma infection. Identity and
672 purity of the human cell lines used in this study were tested and confirmed using STR
673 authentication.

674

675 - *Generation of RPE-1 GFP-H3 WT and GFP-H3S10A stable cell lines:*

676 RPE-1 cells were transfected with 10µg GFP-H3 WT and GFP-H3S10A[1] using JET PRIME kit
677 (Polyplus Transfection, 114-07) according to the manufacturer's protocol. After 24hrs,
678 500µg/ml G418 (4727878001 from Roche) was added to the cell culture medium. After 72hrs
679 of antibiotic selection GFP-positive cells were then collected using Sony SH800 FACS (BD
680 FACSDiva Software Version 8.0.1).
681 GFP-H3 WT and GFP-H3S10A plasmids were a gift of Epstein JA[1].

682

683 - *Generation of RPE-1 GFP-Lamin and mCherry H2B stable cell line:*

684 RPE-1 mCherry cells[2] were transfected with 10µg GFP Lamin chromobodies (Icg from
685 Chromotek) using JET PRIME kit (Polyplus Transfection, 114-07) according to the
686 manufacturer's protocol. After 24hrs, 500µg/ml G418 was added to the cell culture medium.
687 After 72hrs of antibiotic selection mCherry-H2B and GFP-positive (Lamin chromobodies) cells
688 were then collected using Sony SH800 FACS (BD FACSDiva Software Version 8.0.1).

689

690 **Transgenic Animals:**

691 For animal care, we followed the European and French National Regulation for the Protection
692 of Vertebrate Animals used for Experimental and other Scientific Purposes (Directive 2010/63;
693 French Decree 2013-118). The project was authorized and benefited from guidance of the
694 Animal Welfare Body, Research Centre, Curie Institute. All mice were kept in the Curie Institute
695 Specific Pathogen Free (SPF) animal facility for breeding. The transgenic R26-H2B-mCherry
696 mouse line[3] was back-crossed in our animal facility on a C57Bl6/N genetic background

697 (Charles River, France). Only heterozygous R26-H2B-mCherry +/- and control littermate males
698 between 3 and 6 months of age were included in the analysis. Animals were anaesthetized by
699 inhalation of isoflurane (Baxter, DDG9621) before being sacrificed by cervical dislocation for
700 bone tissue collection.
701
702 **Mouse Megakaryocyte *in vitro* differentiation and cell culture:**
703 - *Hematopoietic progenitor enrichment*
704 Tibias and femurs from 2 to 6-months old mice were dissected from the mouse and excess
705 tissue was removed using scalpels. One epiphyse of each bone was cut ant the opened bone
706 was placed into a 1.5mL centrifugation tube containing a 200uL tip. The bones were then
707 centrifuged at high speed during 10 seconds in an Eppendorf tube to eject the bone marrow
708 cells. The cells were resuspended in 1ml of cold RPMI containing 10% fetal bovine serum (GE
709 Healthcare), 100 U/ml penicillin, 100 U/ml streptomycin (15140-122 from Gibco), Anti-Anti
710 (11570486 from Gibco) - hereafter called complete RPMI medium - and centrifuged for 5min
711 at 1700rpm, 4°C.
712 125µl of cold complete RPMI medium were used to resuspend the cells, then 25µl of anti-
713 CD117 magnetic beads (130-097-146 from Miltenyi Biotec) were added and mix to the cells.
714 Cells were incubated on ice for 30min with the beads. Then, 1ml of cold complete RPMI
715 medium was added to the cells and they were filtered through a 100µm cell strainer (431752
716 from Coning) into 50ml tubes. The tubes and the cell strainers were washed with an additional
717 1ml of cold complete RPMI medium. Cells were centrifuged for 5min at 1700rpm, 4°C. During
718 the centrifugation, a MS column (130-042-201 from Miltenyi Biotec) was prewet with 2ml of
719 cold complete RPMI medium and installed on MACS magnet (130-042-501 from Miltenyi
720 Biotec). The cells were then resuspended in 1ml of cold complete RPMI medium and
721 transferred to a 2ml tube. Using an insulin syringe fitted with a short 25G needle (300400 from
722 BD Bioscience), cells were transferred to the column. After, the tubes and the columns were
723 washed using 2ml of cold complete RPMI medium. The CD117-positive fraction was then
724 collected in a tube by pouring the cells using a plunger. The CD117-positive cells were
725 centrifuge for 5min at 1700rpm, 4°C and resuspended in 500µl of cold complete RPMI medium.
726
727 - *Cell culture and In vitro differentiation:*
728 Purified CD117-positive cells were cultured on coverslips pre-treated with PolyLysine
729 (0.02mg/ml during 5', 37°C; HY-126437B from MedChemExpress) and Fibronectin (20µL in
730 500µl PBS, ON 37°C; F1141-5MG from Sigma-Aldrich) in DMEM-F12 + 10% fetal bovine
731 serum (GE Healthcare) + 100 U/ml penicillin, 100 U/ml streptomycin (15140-122 from Gibco).
732 Cells were maintained at 37°C in a 5% CO_2 atmosphere. Megakaryocyte differentiation was

733 induced by adding mSCF (50 ng/mL; 250-03 from Peprotech) + mTPO (50 ng/mL; 315-14 from
734 Peprotech) for at least 3 days.
735
736 **Isolation of mouse Hepatocytes:**
737 Two old C57B6J mice were anesthetized with an intra-peritoneal injection of 10 mg/kg xylazine
738 and 100 mg/kg ketamine. Primary hepatocytes were isolated by the two-step liver collagenase
739 perfusion method and seeded in complete medium, as described previously[4]. Briefly, after
740 caudal vena cava catheterization and portal vein opening, livers were washed with 50 mL of
741 perfusion solution containing 10 mM 4-(2-hydroxyethyl)-1-piperazineethanesulfonic acid
742 (HEPES, Merck #H6147), 137 mM NaCl (Merck #5886), 2.68 mM KCl (Merck #P5405), 232
743 µM Na2HPO4 (Merck #S5136), 0.5 mM ethylenediaminetetraacetic acid (EDTA, Thermo
744 Fisher Scientific #15575020) dissolved in deionized sterile water. Then, livers were digested
745 with a collagenase solution containing 0.5 mg/mL of collagenase type IV (from Clostridium
746 histolyticum, Merck #C5138) diluted in perfusion solution, and 10 mM of CaCl2 (Merck
747 #C7902). After isolation, hepatocytes were collected, washed, and resuspended in complete
748 medium: William's E medium GlutaMAX (Thermo Fisher Scientific #32551020) supplemented
749 with bovine serum albumin 0,1% (Merck #A8412), penicillin-streptomycin 100 U/mL (Thermo
750 Fisher Scientific #15140122), fungizone B 100 µg/mL (Thermo Fisher Scientific #15290026),
751 dexamethasone 25 nM (Merck #D2915) and supplemented with 10% decomplemented foetal
752 bovine serum (FBS, Thermo Fisher Scientific #10270106). The cell viability was equivalent in
753 all groups (≥ 85%) as assessed by the Trypan blue exclusion method. Hepatocytes were
754 seeded at a density of 6.0e+5 in 6-cm dishes and incubated at 37°C under an atmosphere
755 containing 5% (v/v) CO2, for 4 hours, to allow the cells to adhere. The medium was then
756 replaced with fresh FBS-free complete medium which remained unchanged for the 24h of
757 primary culture.
758
759 **Fly husbandry and fly stocks**
760 Flies were raised on cornmeal medium (0.75% agar, 3.5% organic wheat flour, 5.0% yeast,
761 5.5% sugar, 2.5% nipagin, 1.0% penicillin-streptomycin and 0.4% propionic acid). Fly stocks
762 were maintained at 18 °C. Stocks used in this study: w[1118] (3605 from Bloomington).
763 In all experiments, larvae were staged to obtain comparable stages of development. Egg
764 collection was performed at 25 °C for 24 h. After development at 25 °C, third instar larvae were
765 used for dissection.
766
767 **Treatments:**
768 - *Chemicals*

769 The drugs were used at the following concentrations: Auxin (I5148 from Sigma), 500µM;
770 Doxycycline (D3447 from Sigma), 2µg/ml; Asunaprevir (S4935 from Selleckchem), 3µM;
771 Monastrol (S8439 from Selleckchem), 50µM; MPI-0479605 (S7488 from Selleckchem), 1µM;
772 Blebbistatin (B0560 from Sigma), 20µM; Palbociclib (S1579 from Selleckchem), 1µM;
773 Methylstat (HY-15221 from Medchem), 2 (for live imaging or megakaryocytes) or 4µM (for fixed
774 cells); JIB (HY-13953 from MedChemExpress), 2,5 (for megakaryocytes) or 5µM (for human
775 cell lines), Nocodazole (HY-13520 from Medchem), 2µM; Taxol (T1912 from Sigma), 1nM;
776 SP600125 (HY-12041 from Medchem), 20µM; RO3306 (HY-12529 from Medchem), 10µM;
777 Calyculin A (HY-18983 from Medchem), 5nM; C646 (HY-13823 from Medchem), 30µM.
778
779 Methylstat, JIB and C646 were added 6hrs before the induction of whole genome duplication.
780 Nocodazole and Taxol were added 2hrs before the induction of whole genome duplication.
781 Cells were treated with Calyculin A for 2:30hrs before fixation.
782 Megakaryocytes were incubated with Methylstat and JIB for 6hrs three days after the addition
783 of the cytokines. To analyze megakaryocytes that performed mitotic slippage in the presence
784 of the drugs only the small megakaryocytes were considered.
785
786
787 - *Induction of WGD in human cell lines*
788 To induce mitotic slippage, cells were incubated with DMSO (D8418 from Sigma Aldrich) or
789 with a combination of 50µM Monastrol (S8439 from Selleckchem) + 1µM MPI-0479605 (S7488
790 from Selleckchem) for at least 4hrs.
791 Alternatively, to induce mitotic slippage, CCNB1 depletion in RPE CCNB1^{AID} cells was induced
792 as described before[5]. Briefly, cells were treated with 2µg/ml Doxycycline (D3447 from Sigma
793 Aldrich) + 3µM Asunaprevir (S4935 from Selleckchem) for 2hrs. Then, 500 µM Auxin (I5148
794 from Sigma Aldrich) was added to the cell culture medium for at least 4hrs.
795 Mitotic slippage was induced using the combination of Monastrol + MPI-0479605 unless it is
796 specified in the figure legends.
797
798 To induce cytokinesis failure, cells were incubated with DMSO (D8418 from Sigma Aldrich) or
799 with 20µM Blebbistatin (B0560 from Sigma) or with 20µM Paprotrain (HY-101298 from
800 Medchem) for at least 4hrs. Actin staining using Phaloidin (A30107 from ThermoFisher) was
801 used to ascertain the binucleation of the CF-generated tetraploid cells.
802 Cytokinesis failure was induced using Blebbistatin unless it is specified in the figure legends.
803
804 To induce endoreplication, cells were incubated with DMSO (D8418 from Sigma Aldrich) or
805 with 20µM SP600125 (HY-12041 from Medchem) for at least 4hrs.

806 Alternatively, to induce endoreplication, CCNA2 depletion in RPE CCNA2^{AID} cells was induced
807 as described before[5]. Briefly, cells were treated with 2µg/ml Doxycycline (D3447 from Sigma
808 Aldrich) + 3µM Asunaprevir (S4935 from Selleckchem) for 2hrs. Then, 500 µM Auxin (I5148
809 from Sigma Aldrich) was added to the cell culture medium for at least 4hrs.
810 Endoreplication was induced using SP600125 unless it is specified in the figure legends.
811
812 Each treatment generates a mixed population of diploid and tetraploid cells. After
813 synchronizing cells in G1 (see the "Cell cycle synchronization" section), diploid (2N) and
814 tetraploid (4N) cells are easily distinguished based on their nuclear size measured using Image
815 J software V2.1.0/1.53c, https://imagej.net/software/fiji/downloads, as previously described[2].
816
817 - *Cell cycle synchronization*
818 To obtain a synchronous population of G1 cells, after 4hrs of WGD induction (see "Induction
819 of WGD in human cell lines" section) 1µM Palbociclib (Cdk4/6 inhibitor, S1579 from
820 Selleckchem) was added to the cell culture media for 16hrs to synchronize cells at the G1/S
821 transition.
822 To analyze the first G2 upon WGD, Palbociclib was washed five times using PBS 1X and cells
823 were released in the presence of 10µM RO-3306 (HY-12529 from Medchem) to block them in
824 G2.
825 To analyze asynchronous cells, WGD induction was done during 4hrs before to fix the cells.
826
827 **Immunofluorescence:**
828 - *Preparation and imaging of human cells*
829 Cells were plated on cover slips in 12-well plates and treated with the indicated drugs. To label
830 cells, they were fixed using 4% of paraformaldehyde (15710 from Electron Microscopy
831 Sciences) + Triton X-100 (2000-C from Euromedex) 0,1% in PBS (20 min at 4°C) or for
832 alternative H3K9me2 staining with 100% cold Methanol (32213 from Honeywell) (10min at -
833 20°C). Then, cells were washed three times using PBS-T (PBS 1X + 0,1% Triton X-100 +
834 0,02% Sodium Azide) and incubated with PBS-T + BSA (04-100-812-C from Euromedex) 1%
835 for 30 min at RT. After three washes with PBS-T + BSA, primary and secondary antibodies
836 were incubated in PBS-T + BSA 1% for 1hr and 30 min at RT, respectively. After two washes
837 with PBS, cells were incubated with 3 µg/ml DAPI (4',6-diamidino-2-phenylindole; D8417 from
838 Sigma Aldrich) for 15 min at RT. After two washes with PBS, slides were mounted using 1.25%
839 n-propyl gallate (Sigma, P3130), 75% glycerol (bidistilled, 99.5%, VWR, 24388-295), 23.75%
840 H2O.
841 Images were acquired on an upright widefield microscope (DM6B, Leica Systems, Germany)
842 equipped with a motorized XY and a 40X objective (HCX PL APO 40X/1,40-0,70 Oil from

843 Leica). Acquisitions were performed using Metamorph 7.10.1 software (Molecular Devices,
844 USA) and a sCMOS camera (Flash 4V2, Hamamatsu, Japan). Stacks of conventional
845 fluorescence images were collected automatically at a Z-distance of 0.5 µm (Metamorph 7.10.1
846 software; Molecular Devices, RRID:SCR_002368).
847 For H3.1/2 and H3.3 staining, two additional extractions were done, a pre-extraction (Triton X-
848 100, 0,1%, 30sec) before the fixation and a post-extraction (Triton X-100, 0,5%, 5min) after
849 the fixation.
850
851 - *Preparation and imaging of mouse megakaryocytes and mouse hepatocytes*
852 For megakaryocytes, cells were plated on cover slips in 24-well plates and fixed using 4% of
853 paraformaldehyde (15710 from Electron Microscopy Sciences) + Triton X-100 (2000-C from
854 Euromedex) 0,1% in PBS (20 min at RT) or for microtubule staining with 100% cold MetOH
855 (32213 from Honeywell) (10min -20°C). For hepatocytes, cells were plated on cover slips in 6-
856 well plates and fixed using 4% of paraformaldehyde (15710 from Electron Microscopy
857 Sciences) or for microtubule staining with 100% MetOH (32213 from Honeywell) (10min -
858 20°C).
859 Then, cells were washed three times using PBS-T (PBS 1X + 0,1% Triton X-100 + 0,02%
860 Sodium Azide) and incubated with PBS-T + 1% BSA (04-100-812-C from Euromedex) 1% for
861 30 min at RT. After three washes with PBS-T + BSA, primary and secondary antibodies were
862 incubated in PBS-T + BSA 1% for 3hrs and 2hrs at RT, respectively. After two washes with
863 PBS, cells were incubated with 3 µg/ml DAPI (4',6-diamidino-2-phenylindole; D8417 from
864 Sigma Aldrich) for 15 min at RT. After two washes with PBS, slides were mounted using 1.25%
865 n-propyl gallate (Sigma, P3130), 75% glycerol (bidistilled, 99.5%, VWR, 24388-295), 23.75%
866 H2O.
867 Images were acquired on a spinning disk microscope (Gataca Systems, France). Based on a
868 CSU-W1 (Yokogawa, Japan), the spinning head was mounted on an inverted Eclipse Ti2
869 microscope equipped with a motorized XY Stage (Nikon, Japan). Images were acquired
870 through a 100x 1.4NA Plan-Apo objective with a sCMOS camera (Prime95B, Photometrics,
871 USA). Optical sectioning was achieved using a piezo stage (Nano-z series, Mad City Lab,
872 USA). Gataca Systems' laser bench was equipped with 405, 491 and 561 nm laser diodes,
873 delivering 150 mW each, coupled to the spinning disk head through a single mode fibre. Multi-
874 dimensional acquisitions were performed using Metamorph 7.10.1 software (Molecular
875 Devices, USA).
876
877 - *Preparation and imaging of Drosophila salivary glands*
878 *Drosophila* salivary glands from third instar larvae were dissected in PBS and fixed for 30 min
879 in 4% paraformaldehyde in PBS. They were washed 3 times in PBST 0.3% (PBS, 0.3% Triton

880 X-100, T9284 from Sigma), 15 min for each wash, and incubated for 1 hr with blocking solution
881 (PBS, 0.3% Triton X-100 + 5% normal goat serum, 10098792 from Gibco). Then salivary
882 glands were washed 3 times in PBS, 15 min for each wash and incubated overnight at 4 °C
883 with primary antibodies at the appropriate dilution in the blocking solution. Tissues were
884 washed three times in PBST 0.3%, 15 min for each wash, and incubated overnight at 4 °C with
885 secondary antibodies diluted in the blocking solution. Salivary glands were then washed 3
886 times in PBST 0.3%, 15 min for each wash, rinsed in PBS and incubated with 3 µg ml−1 DAPI
887 (4′,6-diamidino-2-phenylindole; Sigma Aldrich D8417) at room temperature for 30 min. Salivary
888 glands were then washed in PBS at room temperature for 30 min and mounted in clearing
889 solution (Rapiclear 1.49 Sunjin Lab, RC149002).
890 Images were acquired as previously described in the section "*Preparation and imaging of*
891 *mouse megakaryocytes and mouse hepatocytes"*.
892
893 - *Structural illumination microscopy:*
894 Images were acquired as previously described in the section "*Preparation and imaging of*
895 *mouse megakaryocytes and mouse hepatocytes"*.
896 Super resolution was achieved on the CSU-W1 spinning disk equipped with a super-resolution
897 module (Live-SR, Gataca systems). This module is based on structured illumination with
898 optical reassignment technique and online processing leading to a two-time resolution
899 improvement. The method called multifocal SIM (MSIM) allows combining the doubling
900 resolution together with the physical optical sectioning of confocal microscopy.
901
902 - *Primary and secondary antibodies*
903 Primary and secondary antibodies were used at the following concentrations: β-catenin (1/250;
904 C2206 from Sigma-Aldrich, RRID:AB_476831), Lamin A/C (1/500; SAB4200236 from Sigma
905 Aldrich, RRID:AB_10743057), Lamin B1 (1/500; ab16048 from Abcam, RRID:AB_443298),
906 H3S10 (1/500, ab14955 from Abcam, RRID:AB_443110), Lamin A/C (1:50, ADL101 from
907 DHSB, RRID:AB_528332), Lamin B (1/50, ADL67.10 from DHSB, RRID:AB_528336), H3K9ac
908 (1/500, 9649S from Ozyme; RRID:AB_823528), H3K14ac (1/500, ab52946 from Abcam,
909 RRID:AB_880442); H3K27ac (1/500, 39685 from Active Motif, RRID:AB_2793305), DM1A
910 (1/1000, T9026 from Sigma Aldrich, RRID:AB_477593), H3K9me2 (1/500, 39239 from Active
911 Motif, RRID:AB_2793199), H3K9me2 (1/500, ab1220 from Abcam; RRID:AB_449854),
912 H3K9me3 (1/500, ab8898 from Abcam, RRID:AB_306848), H3K27me3 (1/500, 39155 from
913 Active motif, RRID:AB_2561020), HP1α (1/500, ab109028 from Abcam, RRID:AB_10858495),
914 Lap2β (1/250, 611000 from BD Bioscience, RRID:AB_398313), LBR (1/500, ab232731 from
915 Abcam, RRID:AB_3246426), Nuclear Pore Complex (1/250, ab24609 from Abcam,
916 RRID:AB_448181), Emerin (1/150, 10351-1-AP from ProteinTech, RRID:AB_2100056), goat

917 anti-Rabbit IgG (H+L) Highly Cross-Adsorbed Secondary Antibody, Alexa Fluor 647 (1/250;
918 A21245 from ThermoFisher, RRID:AB_2535813), Goat anti-Rabbit IgG (H+L) Highly Cross-
919 Adsorbed Secondary Antibody, Alexa Fluor 546 (1/250; A-11035 from ThermoFisher,
920 RRID:AB_2534093), Goat anti-Mouse IgG1 Cross-Adsorbed Secondary Antibody, Alexa
921 Fluor™ 488 (1/250, A-21121 from ThermoFisher, RRID:AB_2535764), Goat anti-Mouse IgG2b
922 Cross-Adsorbed Secondary Antibody, Alexa Fluor™ 488 (1/250, A-21141 from ThermoFisher,
923 RRID:AB_2535778), Goat anti-Mouse IgG2a Cross-Adsorbed Secondary Antibody, Alexa
924 Fluor™ 546 (1/250, A-21133 from ThermoFisher, RRID:AB_2535772), Alexa Fluor™ Plus 647
925 Phalloidin (1/2000, A30107 from ThermoFisher).
926
927 **3D cultures:**
928 - *Mitotic slippage on 3D cultures*
929 To generate spheroids, 500 cells per well were seeded into 96 ultra-low attachment well plates
930 (7007 from Corning) in presence of DMSO (D8418 from Sigma Aldrich) or with 50µM monastrol
931 (S8439 from Selleckchem) and 1µM MPI-0479605 (S7488 from Selleckchem). Plates were
932 spun down at 200g for 3min, to allow spheroid formation, and incubated for 24hrs at 37°C.
933
934 - *Immunostaining*
935 Spheroids were collected and washed quickly with PBS prior fixation using 4% of
936 paraformaldehyde (15710 from Electron Microscopy Sciences) in PBS for 40min. Then,
937 spheroids were permeabilized for 5 min using Triton X-100 (2000-C from Euromedex) 0,3% in
938 PBS and blocked for 30min using Blocking Buffer (BB= PBS 1X + 0,3% Triton X-100 + 0,02%
939 Sodium Azide + 3% BSA). Aggregates were incubated with primary antibodies diluted into BB
940 O/N. After 3 washes using BB, spheroids were incubated with secondary antibodies in BB for
941 3hrs. Cells were then washed several times for 2hrs in BB and mounted on glass with EverBrite
942 (Biotium). For primary and secondary antibodies see *Immunofluorescence microscopy and*
943 *antibodies* section.
944
945 **Time lapse microscopy:**
946 Cells were plated on a dish (627870 from Greiner). Methylstat (2µM) or Nocodazole (2µM)
947 were added two hours before to start the movies. To follow microtubules or actin, SPY650-
948 Tubulin (SC503 from Tebubio) or SPY650-FastAct (SC505 from Tebubio), respectively, were
949 added one hour before to start the movie.
950 Images were acquired on a spinning disk microscope (Gataca Systems, France). Based on a
951 CSU-W1 (Yokogawa, Japan), the spinning head was mounted on an inverted Eclipse Ti2
952 microscope equipped with a motorized XY Stage (Nikon, Japan). Images were acquired
953 through a 40X NA 1.3 oil objective with a sCMOS camera (Prime95B, Photometrics, USA).

954 Optical sectioning was achieved using a piezo stage (Nano-z series, Mad City Lab, USA).
955 Gataca Systems' laser bench was equipped with 405, 491 and 561 nm laser diodes, delivering
956 150 mW each, coupled to the spinning disk head through a single mode fiber. Laser power
957 was chosen to obtain the best ratio of signal/background while avoiding phototoxicity. Multi-
958 dimensional acquisitions were performed using Metamorph 7.10.1 software (Molecular
959 Devices, USA). Stacks of conventional fluorescence images were collected automatically at a
960 Z-distance of 0.5 µm (Metamorph 7.10.1 software; Molecular Devices, RRID:SCR_002368).
961 Images are presented as maximum intensity projections generated with ImageJ software
962 (RRID:SCR_002285), from stacks deconvolved with an extension of Metamorph 7.10.1
963 software.
964
965 **FACS of diploid and tetraploid cells:**
966 A mix of diploid and tetraploid cells synchronized in G1 or in G2/M (see "Cell cycle
967 synchronization" section) were incubated with 2 µg ml−1 Hoescht 33342 (Sigma Aldrich
968 94403) for 1 h at 37 °C, 5% CO2. Then, a single cell suspension was generated. Cells were
969 washed using PBS, the supernatant was removed, and cells were resuspended in cell culture
970 medium containing 1µM EDTA (10135423 from Invitrogen). Fluorescence-activated cell
971 sorting (FACS) was performed using Sony SH800 FACS (BD FACSDiva Software Version
972 8.0.1), as previously described[2]. Compensations were performed using the appropriate
973 negative control samples.
974
975 **HiC experiment:**
976 Diploid and tetraploid cells were isolated using flow cytometry (see "FACS of diploid and
977 tetraploid cells" section). Diploid and tetraploid cells were isolated using flow cytometry (see
978 "FACS of diploid and tetraploid cells" section). Library preparation for Hi-C was conducted as
979 previously described[6]. Briefly, the cells were fixed with formaldehyde, and fixed nuclei were
980 extracted for further processing. Chromatin was digested with MboI restriction enzyme (New
981 England Biolabs, R0147), and digested ends were biotinylated. Next, a proximity ligation was
982 carried out, followed by chromatin crosslink reversal. DNA was purified, sheared via sonication,
983 and size-selected for library preparation. Biotin-marked DNA fragments were pulled down with
984 Dynabeads MyOne Streptavidin C1 (Thermo Fisher Scientific, 65001). Hi-C library preparation
985 continued with end polishing, A-tailing, and Illumina TruSeq unique dual indexes ligation
986 reactions. Lastly, libraries were amplified via PCR, and sequenced on an Illumina HiSeq X
987 platform, PE150 configuration.
988
989 **Atomic force microscopy:**

990 Atomic Force Microscopy measurements were performed on glass bottom dishes (ibidi) with
991 a JPK NanoWizard 4 (Bruker Nano) microscope mounted on an Eclipse Ti2 inverted
992 fluorescent microscope (Nikon) and operated via JPK SPM Control Software v.6. MLCT
993 triangular silicon nitride cantilevers (Bruker) were used to access the mechanical properties of
994 nuclei. Forces of up to 2 nN were applied at 10 micron per second constant cantilever velocity
995 also ensuring an indentation depth of at ~500 nm.
996
997 **ATACseq**
998 - *Sample preparation*
999 The samples were prepared using the following kit 53150 from Active Motif and according to
1000 the manufacturer's protocol. We isolated diploid and tetraploid G1 cells using flow cytometry
1001 (see "FACS of diploid and tetraploid cells" section) and used 1 x10^5 cells per condition. Spike
1002 in (53154 from Active Motif) was added according to the manufacturer's protocol.
1003
1004 - *Sequencing*
1005 The pool was quantified by qPCR using the KAPA library quantification kit (Roche).
1006 Sequencing was carried out on the NovaSeq X Plus instrument from Illumina based on a 2*100
1007 cycle mode (paired-end reads, 100 bases) targeting around 50 million clusters per sample.
1008
1009 **Total RNAseq:**
1010 - *RNA preparation*
1011 Diploid and tetraploid G1 cells were isolated using flow cytometry (see "FACS of diploid and
1012 tetraploid cells" section). Then RNA was extracted using All Prep DNA/RNA Mini Kit (80204
1013 from Qiagen) according to the manufacturer's protocol. To normalize, RNA Spike-in were
1014 added to the samples (4456740 from Invitrogen) according to the manufacturer's protocol. 1 x
1015 10^6 cells were used per condition (3n).
1016 To control the quality of the samples before High-Throughput Sequencing, RNAs were
1017 analyzed to quantify the RIN using Agilent RNA 6000 Nano Kit (5067-1511 from Agilent).
1018
1019 - *Sequencing*
1020 We prepared RNA sequencing libraries from 500ng of total RNA using the Illumina® Stranded
1021 Total RNA Prep and the Ligation with Ribo-Zero Plus library preparation kit, which allows to
1022 perform a strand specific sequencing. This protocol includes a first step of enzymatic depletion
1023 of abundant transcripts from multiple species using specific probes. We then perfomed cDNA
1024 synthesis and used resulting fragments for dA-tailing followed by ligation of RNA Index
1025 Anchors. PCR amplification with indexed primers (IDT for Illumina RNA UD Indexes) was
1026 finally achieved, with 13 cycles, to generate the final cDNA libraries. Individual library

1027 quantification and quality assessment was performed using Qubit fluorometric assay
1028 (Invitrogen) with dsDNA HS (High Sensitivity) Assay Kit and LabChip GX Touch using a High
1029 Sensitivity DNA chip (Perkin Elmer). Libraries were then equimolarly pooled and quantified by
1030 qPCR using the KAPA library quantification kit (Roche). Sequencing was carried out on the
1031 NovaSeq X Plus instrument from Illumina using paired-end 2 x 100 bp, to obtain around 100
1032 million clusters (200 million raw paired-end reads) per sample.
1033

1034 **QUANTIFICATION AND STATISTICAL ANALYSIS**

1035

1036 **Immunofluorescence:**

1037 Image analysis and quantifications were performed using Image J software V2.1.0/1.53c,
1038 https://imagej.net/software/fiji/downloads[7]. Images are presented as maximum intensity
1039 projections generated with ImageJ software (RRID:SCR_002285).

1040 For the 3D reconstruction, images were converted in Imaris files using ImarisFileConverter
1041 9.9.1 (Bitplane, RRID:SCR_007370). Then, images were imported into Imaris software v.9.6.0
1042 (Bitplane, RRID:SCR_007370). Nuclear shapes were reconstructed based on the DNA
1043 staining. 3D views were generated using Imaris software and saved as TIFF.

1044 To quantitatively measure nuclear shapes, the "wand" tool from Image J V2.1.0/1.53c software
1045 was used to select the nuclei based on the DAPI staining and then the circularity and solidity
1046 indexes were measured using the "shape descriptors" tool from Image J V2.1.0/1.53c software.

1047 To quantify fluorescence intensity, images were converted into maximum intensity projections
1048 and the mean fluorescence intensity at the whole nucleus was measured using the "polygon
1049 sections" tool from Image J V2.1.0/1.53c software while the mean fluorescence intensity at the
1050 nuclear envelope or locally at the intact/deformed regions were measured using the
1051 "segmented lines" tool from Image J V2.1.0/1.53c software. Since diploid cells were not
1052 deformed, the mean fluorescence intensity was compared at two random regions to visualize
1053 the distribution of the signal, while in newly born tetraploid cells, intact and deformed areas
1054 were compared.

1055 The coefficient of variation (CoV) was measured by dividing the standard deviation of the signal
1056 by the mean fluorescence intensity for each cell.

1057 To define small and large megakaryocytes or hepatocytes, the median nuclear size was used
1058 as a threshold.

1059 For the figures, images were processed on Image J V2.1.0/1.53c software, and mounted using
1060 Affinity Designer 2, https://affinity.serif.com/fr/designer/.

1061

1062 **Time lapse microscopy:**

1063 Image analysis and quantifications were performed using Image J software V2.1.0/1.53c,
1064 https://imagej.net/software/fiji/downloads. Videos were corrected using "3D correct drift" plugin
1065 with Image J V2.1.0/1.53c software to keep the cell of interest at the center of the region of
1066 interest.

1067 For the Figure 2D, nuclei masks were generated using the Fiji Plugin as described in[8]. Briefly,
1068 this process involves denoising (using the Pure Denoise Fiji Plugin[9]) and thresholding the
1069 image over time, to get one ROI (the nucleus) on each frame. A custom macro was then used
1070 to project the contours over time, with each contour colored according to its corresponding

1071 frame. The Analyze Particles function was applied to the masks generated by the Plugin, and
1072 the contours' ROIs were color-coded according to their frame using BAR Plugin.
1073 To analyze nuclear shapes by live imaging, single cells were followed, and nuclear circularity
1074 and solidity indexes were measured in G2 before the NEBD and in G1 after complete DNA
1075 decondensation. The results were plotted using the "before-after" representation from
1076 GraphPad Prism (RRID:SCR_002798) version 10 for Mac, GraphPad Software, La Jolla
1077 California USA, www.graphpad.com. The delta circularity was measured by dividing the
1078 nuclear circularity index in G2 by the one in G1 for each single cell.
1079 For the figures, images were processed on Image J V2.1.0/1.53c software, and mounted using
1080 Affinity Designer 2, https://affinity.serif.com/fr/designer/.
1081
1082 **Total RNAseq data:**
1083 Analysis of sequencing data quality, reads repartition (e.g., for potential ribosomal
1084 contamination), inner distance size estimation, genebody coverage, strand-specificity of library
1085 were performed using FastQC, Picard-Tools, Samtools, and RSeQC. Reads were mapped
1086 using STAR on the Human hg38 genome assembly and read count was performed using
1087 featureCount from SubRead and the Human FAST DB v2022_1 annotations.
1088 Gene expression was estimated as described previously[10]. Only genes expressed in at least
1089 one of the two compared conditions were analyzed further. Genes were considered as
1090 expressed if their FPKM value was greater than FPKM of 98% of the intergenic regions
1091 (background). Analysis at the gene level was performed using DESeq2[11]. Genes were
1092 considered differentially expressed for fold-changes ≥ 1.5 and p-values ≤ 0.05.
1093 Overrepresented analyses and GSEA[12] were performed using WebGestalt[13] merging results
1094 from up-regulated and down-regulated genes only, as well as all regulated genes. Pathways
1095 and networks were considered significant with p-values ≤ 0.05.
1096 VolcanoPlots were created using ggplot2. In blue are genes that are differentially under-
1097 expressed in the Tetraploid condition, and in red those that are over-expressed (based on
1098 thresholds indicated after the use of DESeq2).
1099
1100 **ATACseq:**
1101 Quality control was performed using FastQC and MultiQC. Sequencing reads were aligned to
1102 the human reference genome (hg38) using the BWA-MEM2 algorithm. Duplicate reads were
1103 marked using the Picard MarkDuplicates tool. Only reads with a mapping quality score ≥40
1104 were retained, using Samtools. Spike-in normalization was conducted following the guidelines
1105 provided by ActiveMotif. Briefly, the number of reads uniquely mapped to the Drosophila (dm6)
1106 genome was quantified per sample. A normalization ratio was then calculated based on the
1107 lowest number of Drosophila-mapped reads among all samples. This ratio was subsequently

applied to down sample the uniquely mapped reads to the human genome in each sample with Samtools. Samtools was also used to shift BAM files. Peak calling was performed with MACS3 callpeak. Peaks overlapping ENCODE blacklist regions were removed using subtractBed. Peaks with log2 fold change (log2FC) < 3 and -log10(FDR) < 2 were filtered out. Differential peak analysis was carried out using DiffBind in a replicate mode. Finally, peak annotation was performed using HOMER.

Atomic force microscopy:

Analyses were performed with JPK Data Processing Software v.6 (Bruker Nano) by 1) removing the offset from the baseline of raw force curves, 2) identifying the contact point and subtracting cantilever bending then 3) fitting the Hertz model with correct tip geometry to quantitate the reported Young's Modulus of nuclei.

HiC data:

For Hi-C data, reads were mapped to the human hg19 reference genome. Generation of Hi-C contact maps and further analyses, including inter-chromosomal interactions, intercompartmental interactions, and conservation of insulating boundaries were performed as previously described[6].

Statistical analysis:

The statistical significance of differences was calculated using GraphPad Prism (RRID:SCR_002798) version 10 for Mac, GraphPad Software, La Jolla California USA, www.graphpad.com. The statistical test used for each experiment is indicated in the figure legends. Each representative image originates from the analyzed dataset and are representative of the associated quantifications. ns=not significant. *=P ≤ 0.05. **= P ≤ 0.01. ***= P ≤ 0.001. ****= P ≤ 0.0001.

REFERENCES METHOD SECTION

1. Poleshko, A. *et al.* H3K9me2 orchestrates inheritance of spatial positioning of peripheral heterochromatin through mitosis. *eLife* **8**, e49278 (2019).
2. Gemble, S. *et al.* Genetic instability from a single S phase after whole-genome duplication. *Nature* **604**, 146–151 (2022).
3. Abe, T. *et al.* Establishment of conditional reporter mouse lines at ROSA26 locus for live cell imaging. *Genes. N. Y. N 2000* **49**, 579–590 (2011).
4. Donne, R. *et al.* Replication stress triggered by nucleotide pool imbalance drives DNA damage and cGAS-STING pathway activation in NAFLD. *Dev. Cell* **57**, 1728-1741.e6 (2022).
5. Hégarat, N. *et al.* Cyclin A triggers Mitosis either via the Greatwall kinase pathway or Cyclin B. *EMBO J.* **39**, e104419 (2020).
6. Lambuta, R. A. *et al.* Whole-genome doubling drives oncogenic loss of chromatin segregation. *Nature* **615**, 925–933 (2023).
7. Schindelin, J. *et al.* Fiji: an open-source platform for biological-image analysis. *Nat. Methods* **9**, 676–682 (2012).
8. Almonacid, M. *et al.* Active Fluctuations of the Nuclear Envelope Shape the Transcriptional Dynamics in Oocytes. *Dev. Cell* **51**, 145-157.e10 (2019).
9. Luisier, F., Blu, T. & Unser, M. Image denoising in mixed Poisson-Gaussian noise. *IEEE Trans. Image Process. Publ. IEEE Signal Process. Soc.* **20**, 696–708 (2011).
10. Paillet, J. *et al.* Autoimmunity affecting the biliary tract fuels the immunosurveillance of cholangiocarcinoma. *J. Exp. Med.* **218**, e20200853 (2021).
11. Love, M. I., Huber, W. & Anders, S. Moderated estimation of fold change and dispersion for RNA-seq data with DESeq2. *Genome Biol.* **15**, 550 (2014).
12. Subramanian, A. *et al.* Gene set enrichment analysis: a knowledge-based approach for interpreting genome-wide expression profiles. *Proc. Natl. Acad. Sci. U. S. A.* **102**, 15545–15550 (2005).
13. Liao, Y., Wang, J., Jaehnig, E. J., Shi, Z. & Zhang, B. WebGestalt 2019: gene set analysis toolkit with revamped UIs and APIs. *Nucleic Acids Res.* **47**, W199–W205 (2019).

1168 **FIGURE LEGENDS**
1169
1170 **Figure 1: Unscheduled WGD induced through MS generates cells with nuclear**
1171 **instability**
1172
1173 **(A)** Schematic representations of mitotic division (left panel) and of the different means
1174 employed to generate tetraploid cells (right panel). **(B)** Structural illumination
1175 microscopy (SIM) representative images (top) and their corresponding 3D
1176 reconstructions (bottom) showing nuclear shape in G1 RPE-1 cells upon canonical
1177 mitotic division, MS, CF or EnR. Lamin A/C in yellow, DNA in magenta. **(C)** Schematic
1178 illustration of the circularity and solidity indices. **(D-F)** Graphs showing the nuclear
1179 circularity and solidity indices in RPE-1 G1 cells upon **(D)** EnR (in red), **(E)** CF (in
1180 yellow) and **(F)** MS (in blue). Mean ± SEM, >150 G1 cells analysed per condition, three
1181 independent experiments. **(G)** Stills from time-lapse imaging of RPE-1 cells stably
1182 expressing mCherry-H2B (in magenta) performing mitotic division (upper panel) or MS
1183 (lower panel). **(H)** Graph presenting the nuclear circularity and solidity measured at the
1184 single cell level in the same cells in G2 and in G1 upon mitotic division (in grey) or MS
1185 (in blue). >80 cells analysed per condition, three independent experiments. **(I)** Graph
1186 showing the delta circularity (defined as the difference between nuclear circularity in
1187 G2 vs in G1) upon mitotic division (in grey) or MS (in blue) in RPE-1 cells. Mean ± SEM,
1188 >75 cells analysed per condition, three independent experiments. **(J)** Representative
1189 images showing G1 RPE-1 nuclei upon mitotic division, MS, CF and EnR (upper
1190 panel). DNA in magenta. The nuclear contour is indicated (black dotted line, lower
1191 panel). **(K)** Graph showing the nuclear circularity and solidity index from **(D-F)** in diploid
1192 (in grey) and in tetraploid G1 RPE-1 cells generated by EnR (in red), CF (in yellow)
1193 and MS (in blue). Scale bars: 10µm. WGD=whole genome duplication. D=diploid;
1194 T=tetraploid; MS=mitotic slippage; CF=cytokinesis failure; EnR= endoreplication.
1195 NEBD=nuclear envelope breakdown. A.U.=arbitrary unit. **(D,E,F)** ANOVA test (one-
1196 sided). **(H,I)** t-test (two-sided). ns=not significant. *=P ≤ 0.05. **= P ≤ 0.01. ***= P ≤
1197 0.001. ****= P ≤ 0.0001.
1198

1199 **Figure 2: Mitotic slippage generates tetraploid cells with high histone acetylation**
1200 **levels and softer nuclei promoting nuclear deformations**
1201
1202 **(A)** SIM representative images showing diploid and tetraploid G1 RPE-1 cells
1203 generated by MS or EnR. H3S10 in green, DNA in magenta. **(B)** Graph showing the
1204 H3S10 coefficient of variation (defined as the ratio of the standard deviation to the
1205 mean) in G1 in diploid (in grey) or tetraploid RPE-1 cells generated by MS (in blue) or
1206 by CF (in yellow). Mean ± SEM, >75 cells analysed per condition, three independent
1207 experiments. **(C)** Representative images showing diploid and tetraploid G1 RPE-1 cells
1208 generated by MS and stably expressing H3 WT or H3 S10A. DNA in magenta. **(D)**
1209 Graph showing the nuclear circularity index in diploid (in grey) and in MS-generated
1210 tetraploid (in blue) G1 RPE-1 cells stably expressing H3WT or H3S10A. Mean ± SEM,
1211 >150 cells analysed per condition, three independent experiments. **(E-G)** Graphs
1212 showing H3K9ac, H3K27ac and H3K14ac levels in diploid (in grey) and in tetraploid
1213 G1 RPE-1 cells generated by EnR (**E**, in red), by CF (**F**, in yellow) or by MS (**G**, in
1214 blue). Mean ± SEM, >100 cells analysed per condition, three independent experiments.
1215 **(H)** Volcano plot showing ATACseq data comparing diploid and tetraploid G1 RPE-1
1216 cells generated by MS. **(I)** Left panel - Schematic representation showing the principle
1217 of atomic force microscopy (AFM). Right panel - Representative images showing
1218 diploid and MS-generated tetraploid G1 RPE-1 cells. DNA in magenta. Brightfield in
1219 grey. **(J)** Graph showing nuclear stiffness in diploid (in grey) and in tetraploid G1 RPE-
1220 1 cells generated by MS (in blue) or by CF (in yellow). Box and whiskers ± Min to Max,
1221 >90 cells (left panel) or >65 cells (right panel) analysed per condition, three
1222 independent experiments. **(K)** Representative images showing diploid and tetraploid
1223 G1 RPE-1 cells generated by MS treated with DMSO or Methylstat. DNA in magenta.
1224 **(L)** Graph showing H3K9ac and H3K27ac levels in diploid (in grey) and in MS-
1225 generated tetraploid (in blue) G1 RPE-1 cells treated with DMSO or Methylstat.
1226 Mean ± SEM, >100 cells analysed per condition, three independent experiments. **(M)**
1227 Graph showing the nuclear circularity and solidity indices in diploid (in grey) and in MS-
1228 generated tetraploid (in blue) G1 RPE-1 cells treated with DMSO or Methylstat.
1229 Mean ± SEM, >125 cells analysed per condition, three independent experiments. **(N)**
1230 Graph showing the nuclear circularity and solidity indices from **(M)** in diploid (in grey)
1231 and tetraploid G1 RPE-1 cells generated by MS (in blue) treated with DMSO or
1232 Methylstat. Scale bars: 10µm. D=diploid; T=tetraploid; MS=mitotic slippage.
1233 EnR=endoreplication. CF=cytokinesis failure. A.U.=arbitrary unit. **(J)** Kolmogorov-
1234 Smirnov test. **(E,F,G,L)** t-test (two-sided). **(B,D,M)** ANOVA test (one-sided). ns=not
1235 significant. *=P ≤ 0.05. **= P ≤ 0.01. ***= P ≤ 0.001. ****= P ≤ 0.0001.
1236

1237 **Figure 3: Mitotic slippage promotes local nuclear reorganisation and impairs 3D**
1238 **genome organisation**
1239
1240 **(A-C)** Graphs showing the relative H3K9me2 (left panel) or Lamin B1 vs A/C ratio (right
1241 panel) mean intensity at the nuclear envelope in diploid (in grey) and tetraploid G1
1242 RPE-1 cells generated by EnR (**A**, in red), by CF (**B**, in yellow) or by MS (**C**, in blue).
1243 Mean ± SEM, >100 cells analysed per condition, three independent experiments. **(D)**
1244 Left, schematic representation fluorescence intensity measured at the nuclear
1245 envelope or locally at two random regions (in diploid cells) and at intact and deformed
1246 regions (in tetraploid cells). Middle and right panels, SIM representative images
1247 showing diploid (top) and tetraploid (bottom) G1 RPE-1 cells generated by MS. Lamin
1248 A/C in yellow hot, H3K9me2 in cyan hot, Lamin B1 in red hot. DNA in magenta. **(E)**
1249 Graphs showing the relative H3K9me2 or Lamin B1 vs A/C ratio mean intensity at the
1250 nuclear envelope in diploid (in grey) and in tetraploid G1 RPE-1 cells generated by MS
1251 (in blue) treated with DMSO or Methylstat. Mean ± SEM, >100 cells analysed per
1252 condition, three independent experiments. **(F)** Heatmap of the ratios of
1253 interchromosomal contact enrichments (observed versus expected) between tetraploid
1254 (MS) and diploid G1 RPE-1 cells. Chromosomes were sorted by length. Scale bar:
1255 10µm. D=diploid. T=tetraploid. MS=mitotic slippage. EnR=endoreplication.
1256 CF=cytokinesis failure. NE= nuclear envelope. A.U.=arbitrary unit. (**A,B,C,E**) t-test
1257 (two-sided). ns=not significant. *=P ≤ 0.05. **= P ≤ 0.01. ***= P ≤ 0.001. ****= P ≤
1258 0.0001.
1259

1260 **Figure 4: Megakaryocytes undergo mitotic slippage and display nuclear**
1261 **instability**
1262
1263 **(A)** Left panel - schematic workflow showing the methods used to induce
1264 megakaryocyte (MK) differentiation *in vitro*. Right panel – representative image
1265 showing a large polyploid megakaryocyte surrounded by diploid progenitors. Actin in
1266 grey, DNA in magenta. **(B)** Stills from time-lapse imaging of MKs stably expressing
1267 mCherry-H2B (in magenta). Brightfield in grey. **(C)** SIM representative images and
1268 corresponding 3D reconstructions showing diploid progenitors and polyploid
1269 megakaryocyte. Lamin A/C in yellow, DNA in magenta. **(D-F)** Graphs showing nuclear
1270 circularity and solidity in **(D)** *Drosophila* salivary glands (in red), in **(E)** mouse diploid
1271 (in grey) or polyploid hepatocytes (in yellow) and in **(F)** diploid mouse progenitors (in
1272 grey) and in polyploid megakaryocytes (in blue). Mean ± SEM, **(D)** >200, **(E)** >65, **(F)**
1273 >65 interphase cells analysed per condition, three independent experiments. **(G)**
1274 Representative images of megakaryocyte, hepatocyte or salivary gland nuclei, the
1275 nuclear contour is indicated below. DNA in magenta. **(H)** Graph showing the nuclear
1276 circularity and solidity index from **(D-F)** in *Drosophila* salivary glands (in red), in mouse
1277 diploid (in grey) or polyploid hepatocytes (in yellow) and in diploid mouse progenitors
1278 (in grey) and in polyploid megakaryocytes (in blue). Scale bars: 10µm. MS=mitotic
1279 slippage. EnR=endoreplication. CF=cytokinesis failure. MK=megakaryocytes.
1280 NEBD=nuclear envelope breakdown. A.U.=arbitrary unit. **(D-E)** t-test (two-sided). **(F)**
1281 ANOVA test (one-sided). ns=not significant. *=P ≤ 0.05. **= P ≤ 0.01. ***= P ≤ 0.001.
1282 ****= P ≤ 0.0001.
1283

1284 **Figure 5: Mitotic slippage in megakaryocytes alters chromatin and nuclear**
1285 **envelope composition, promoting nuclear deformation**
1286
1287 **(A)** Representative images of mouse diploid progenitors and polyploid
1288 megakaryocytes. DNA in magenta. H3K27ac (upper panel) and H3K9ac (lower panel)
1289 in cyan hot. **(B)** Graph showing the H3K27ac (left panel) and H3K9ac (right panel)
1290 levels in diploid (in grey) and in polyploid megakaryocytes (in blue). Mean ± SEM, >140
1291 interphase cells analysed per condition, three independent experiments. **(C)**
1292 Representative images of diploid progenitor and polyploid megakaryocytes. Lamin A/C
1293 in yellow hot, Lamin B1 in red hot, DNA in magenta. The dotted line shows the nuclear
1294 contour. **(D)** Lamin A/C mean intensity at the nuclear envelope in diploid (in grey) and
1295 in polyploid megakaryocytes (in blue). Mean ± SEM, >150 interphase cells analysed
1296 per condition, three independent experiments. **(E)** Representative images of diploid
1297 progenitors and polyploid megakaryocytes treated with DMSO or Methylstat. DNA in
1298 magenta. The dotted line shows the nuclear contour. **(F)** Graph showing the nuclear
1299 circularity and solidity indices in diploid progenitors (in grey) and polyploid
1300 megakaryocytes (in blue) treated with DMSO or Methylstat or JIB. Mean ± SEM, >90
1301 interphase cells analysed per condition, three independent experiments. **(G)** Graph
1302 showing the nuclear circularity and solidity index from **(F)** in diploid progenitors (in grey)
1303 and polyploid megakaryocytes (in blue) treated with DMSO or Methylstat. **(H)** MS,
1304 unlike CF and EnR, generated tetraploid cells displaying abnormal nuclear
1305 configurations. These defects include maintenance of high H3S10 phosphorylation
1306 levels in G1, which promotes histone acetylation and thus decreased nuclear stiffness.
1307 Scale bars: 10µm. MK=megakaryocyte. NE=nuclear envelope. A.U.=arbitrary unit.
1308 **(B,D,F)** ANOVA test (one-sided). ns=not significant. *=P ≤ 0.05. **= P ≤ 0.01. ***= P ≤
1309 0.001. ****= P ≤ 0.0001.
1310

1311 **SUPPLEMENTARY FIGURE LEGENDS**
1312
1313 **Figure S1: Mitotic slippage unlike cytokinesis failure or endoreplication,**
1314 **generates polyploid cells with abnormal nuclear architecture**
1315
1316 **(A)** Schematic representation showing the methods used to induce whole genome
1317 duplication. **(B)** Left panel – representative images showing diploid and CF-generated
1318 tetraploid G1 RPE-1 cells. β-Catenin in grey, DNA in magenta. Right panel – Graph
1319 showing nuclear circularity and solidity in diploid and in CF-generated tetraploid G1
1320 RPE-1 cells (in grey and yellow, respectively). Mean ± SEM, >100 G1 cells analysed
1321 per condition, three independent experiments. **(C-D)** Graphs showing nuclear
1322 circularity and solidity in diploid and in **(C)** MS- and **(D)** EnR-generated tetraploid G1
1323 RPE-1 cells (in blue and red, respectively). Mean ± SEM, >150 G1 cells analysed per
1324 condition, three independent experiments. **(E)** Graphs presenting nuclear circularity
1325 and solidity in diploid and in MS-generated tetraploid HCT116 cells in G1 (in grey and
1326 blue, respectively). Mean ± SEM, >100 G1 cells analysed per condition, three
1327 independent experiments. **(F)** Representative images showing diploid and MS-
1328 generated tetraploid HCT116 nuclei. DNA in magenta. **(G)** Graphs showing nuclear
1329 circularity and solidity in diploid and in MS-generated tetraploid BJ cells in G1 (in grey
1330 and blue, respectively). Mean ± SEM, >100 G1 cells analysed per condition, three
1331 independent experiments. **(H)** Representative images presenting diploid and MS-
1332 generated tetraploid BJ nuclei. DNA in magenta. **(I)** Graph showing nuclear circularity
1333 and solidity in diploid and in MS-generated tetraploid RPE-1 cells cultured in 3D (in
1334 grey and blue, respectively). Mean ± SEM, >100 G1 cells analysed per condition, three
1335 independent experiments. **(J)** Representative images showing an RPE-1 spheroid
1336 containing diploid and MS-generated tetraploid cells. Actin in grey, DNA in magenta.
1337 **(K-L)** Graphs showing nuclear circularity and solidity in diploid and in MS-generated
1338 tetraploid **(K)** HCT116 and **(L)** BJ cells cultured in 3D (in grey and blue, respectively).
1339 Mean ± SEM, >110 G1 cells analysed per condition, three independent experiments.
1340 **(M)** Graph showing nuclear circularity and solidity in diploid and in MS-generated
1341 tetraploid asynchronous RPE-1 cells (in grey and blue, respectively). Mean ± SEM,
1342 >110 interphase cells analysed per condition, three independent experiments. **(N-O)**
1343 Graphs presenting nuclear area in diploid and in MS- and EnR-generated tetraploid
1344 **(N)** G1 RPE-1 and **(O)** HCT116 cells (in grey, blue and red, respectively). Mean ± SEM,
1345 >150 G1 cells analysed per condition, three independent experiments. **(P)** Graph
1346 showing nuclear circularity and solidity in diploid and in MS-generated tetraploid G2
1347 RPE-1 cells (in grey and blue, respectively). Mean ± SEM, >170 G2 cells analysed per
1348 condition, three independent experiments. **(Q)** Representative images showing diploid
1349 and MS-generated tetraploid RPE-1 shP53 cells. DNA in magenta. **(R-S)** Graphs
1350 showing nuclear **(R)** circularity and **(S)** solidity in diploid and in MS-generated tetraploid
1351 RPE-1 shp53 cells (in grey and blue, respectively). Mean ± SEM, >100 interphase cells
1352 analysed per condition, three independent experiments. Scale bars: 10µm. D=diploid.
1353 T=tetraploid. MS=mitotic slippage. CF=cytokinesis failure. EnR= endoreplication.
1354 A.U.=arbitrary unit. **(B,C,D,E,G,M,N,O,P,R,S)** Anova-test (one sided). **(I,K,L)** t-test

1355 (two-sided). ns=not significant. *=P ≤ 0.05. **= P ≤ 0.01. ***= P ≤ 0.001. ****= P ≤
1356 0.0001.

1357 **Figure S2: High levels of H3S10 phosphorylation contributes to nuclear deformations**
1358 **upon mitotic slippage**
1359
1360 **(A)** SIM representative images showing diploid RPE-1 mitotic cells. H3S10 in green,
1361 DNA in magenta. **(B)** Graph showing H3S10 mean intensity during mitosis in diploid
1362 RPE-1 cells. Mean ± SEM, >25 mitotic cells analysed per condition, three independent
1363 experiments. **(C)** Graph showing the H3S10 mean intensity in RPE-1 diploid mitotic
1364 cells stably expressing H3 WT and H3 S10A. Mean ± SEM, >65 mitotic cells analysed
1365 per condition, three independent experiments. **(D)** Graph showing the nuclear solidity
1366 in diploid (in grey) and MS-generated tetraploid (in blue) G1 RPE-1 cells stably
1367 expressing H3 WT or H3 S10A. Mean ± SEM, >150 cells analysed per condition, three
1368 independent experiments. **(E)** Graphs showing the nuclear circularity and solidity index
1369 from **(D and Fig. 2D)** in diploid (in grey) and in tetraploid G1 RPE-1 cells (in blue)
1370 generated by MS. **(F)** SIM representative images showing diploid cells treated with
1371 DMSO or 5nM Calyculin. H3S10 in green, DNA in magenta. **(G)** Graphs showing the
1372 nuclear circularity and solidity index in diploid RPE-1 cells treated with DMSO or 5nM
1373 Calyculin. Mean ± SEM, >230 G1 cells analysed per condition, three independent
1374 experiments. Scale bar: 10µm. D=diploid. T=tetraploid. MS=mitotic slippage. NE=
1375 nuclear envelope. A.U.=arbitrary unit. (**B,D**) ANOVA test (one-sided). (**C,G**) t-test (two-
1376 sided). ns=not significant. *=P ≤ 0.05. **= P ≤ 0.01. ***= P ≤ 0.001. ****= P ≤ 0.0001.
1377

1378 **Figure S3: Mitotic slippage, but not cytokinesis failure and endoreplication,**
1379 **alters histone modification**
1380
1381 **(A)** Schematic representation of the mean fluorescence measured at the level of the
1382 whole nucleus in diploid and tetraploid cells. **(B)** SIM representative images showing
1383 diploid and tetraploid G1 RPE-1 cells generated by EnR (left panel), by CF (central
1384 panel) or by MS (right panel). H3K9ac, H3K27ac and H3K14ac in cyan hot. **(C)** Graphs
1385 showing the relative H3K9ac (left panel) or H3K27ac (right panel) mean intensity in the
1386 nucleus in diploid (in grey) and in tetraploid (in blue) RPE-1 G1 cells stably expressing
1387 H3 WT or H3 S10A. Mean ± SEM, >100 G1 cells analysed per condition, three
1388 independent experiments. **(D)** Left panel – SIM representative images showing diploid
1389 and tetraploid G1 RPE-1 cells generated by MS. Lamin A/C in yellow hot, H3K9me2 in
1390 cyan hot and DNA in magenta. Right panel – Graph presenting the relative H3K9me2
1391 mean intensity in the nucleus in diploid (in grey) and in tetraploid (in blue) G1 RPE-1
1392 cells. Mean ± SEM, >100 G1 cells analysed per condition, three independent
1393 experiments. **(E)** Left panel - SIM representative images showing diploid and tetraploid
1394 G1 RPE-1 cells generated by MS. Lamin A/C in yellow hot, H3K9me3 in cyan hot and
1395 DNA in magenta. Right panel – Graph presenting the relative H3K9me3 mean intensity
1396 in the nucleus in RPE-1 diploid (in grey) and in tetraploid (in blue) G1 cells.
1397 Mean ± SEM, >100 G1 cells analysed per condition, three independent experiments.
1398 **(F)** Left panel - SIM representative images showing diploid and tetraploid G1 RPE-1
1399 cells generated by MS. Lamin A/C in yellow hot, H3K27me3 in cyan hot and DNA in
1400 magenta. Right panel – Graph presenting the Relative H3K27me2 mean intensity in
1401 the nucleus in diploid (in grey) and in tetraploid (in blue) G1 RPE-1 cells. Mean ± SEM,
1402 >100 G1 cells analysed per condition, three independent experiments. **(G-H)** Graphs
1403 showing the relative H3K9me2, H3K9me3 and H3K27me3 mean intensity in the
1404 nucleus in diploid (in grey) and in tetraploid G1 RPE-1 cells generated by **(G)** EnR (in
1405 red) or by **(H)** CF (in yellow). Mean ± SEM, >100 G1 cells analysed per condition, three
1406 independent experiments. **(I)** SIM representative images showing diploid and tetraploid
1407 G1 RPE-1 cells generated by MS. HP1α in cyan hot and DNA in magenta. **(J)** Graph
1408 showing the number of HP1 foci / nuclear area in diploid (in grey) and in tetraploid (in
1409 blue) RPE-1 G1 cells. Mean ± SEM, >90 G1 cells analysed per condition, at least three
1410 independent experiments. **(K)** Graph showing nuclear stiffness in diploid and in MS-
1411 generated tetraploid G1 RPE-1 CCNB1 cells (in grey and blue, respectively). Box and
1412 whiskers ± Min to Max, >175 G1 cells analysed per condition, three independent
1413 experiments. Scale bars: 10µm. D=diploid. T=tetraploid. MS=mitotic slippage.
1414 EnR=endoreplication. CF=cytokinesis failure. A.U.=arbitrary unit. **(C,D,E,F,G,H,J)** t-
1415 test (two-sided). **(K)** Kolmogorov-Smirnov test. ns=not significant. *=P ≤ 0.05. **= P ≤
1416 0.01. ***= P ≤ 0.001. ****= P ≤ 0.0001.
1417

Figure S4: Promoting nuclear compaction is sufficient to prevent nuclear deformations upon mitotic slippage

(A) Graphs presenting the relative H3K9ac mean intensity (left panel) or the nuclear area (right panel) in diploid RPE-1 cells. Mean ± SEM, >125 cells analysed per condition, at least three independent experiments. **(B)** Representative images showing RPE-1 diploid cells treated with DMSO or Methylstat. H3K9ac in cyan hot, DNA in magenta. **(C)** Graph showing the nuclear stiffness in diploid (in grey) and tetraploid (in blue) RPE-1 G1 cells generated by MS treated with DMSO or Methylstat. **(D)** Representative images showing diploid and tetraploid RPE-1 G1 cells treated with DMSO or C646. DNA in magenta. **(E)** Graphs showing the nuclear circularity (left panel) and solidity (ritght panel) indicies in diploid (in grey) and tetraploid (in blue) RPE-1 G1 cells generated by MS. Mean ± SEM, >125 G1 cells analysed per condition, at least three independent experiments. **(F)** Graphs presenting the nuclear circularity and solidity from **(E)** in RPE-1 diploid (in grey) and tetraploid (in blue) G1 cells treated with DMSO or C646. **(G)** Representative images showing diploid and tetraploid RPE-1 cells treated with DMSO or JIB. DNA in magenta. **(H)** Graphs presenting the nuclear circularity (left panel) and solidity (ritght panel) indices in diploid (in grey) and tetraploid (in blue) RPE-1 G1 cells generated by MS treated with DMSO or 5μM JIB. Mean ± SEM, >100 G1 cells analysed per condition, at least three independent experiments. **(I)** Graphs presenting the nuclear circularity and solidity from **(H)** in diploid (in grey) and tetraploid (in blue) RPE-1 G1 cells. **(J)** Stills from time-lapse imaging of RPE-1 cells stably expressing mCherry-H2B (in magenta) performing MS and treated with DMSO (upper panel) or Methylstat (lower panel). **(K)** Graphs showing the nuclear circularity (left panel) and solidity (right panel) measured at the single cell levels in G2 and in G1 upon mitotic division (in grey) or MS (in blue) in RPE-1 cells treated with DMSO or 2μM Methylstat. >30 cells analysed per condition, three independent experiments. **(L)** Graph showing the delta circularity (defined as the difference between nuclear circularity in G2 vs in G1) upon mitotic division (in grey) or MS (in blue) in RPE-1 cells treated with DMSO or 2μM Methylstat. Mean ± SEM, >25 cells analysed per condition, three independent experiments. **(M-O)** Graphs displaying nuclear circularity and solidity in **(M)** RPE-CCNB1 or **(N)** BJ or **(O)** HCT116 cells treated with DMSO or Methylstat. Mean ± SEM, >65 G1 cells analysed per condition, three independent experiments. Scale bars: 10μm. D=diploid. T=tetraploid. MS=mitotic slippage. NEBD=nuclear envelope breakdown. A.U.=arbitrary unit**. (A,K,L)** t-test (two-sided). **(E,H,M,N,O)** Anova-test (one-sided). **(C)** Kolmogorov-Smirnov test. ns=not significant. *=P ≤ 0.05. **= P ≤ 0.01. ***= P ≤ 0.001. ****= P ≤ 0.0001.

1460 **Figure S5: The microtubule cytoskeleton contributes to nuclear deformations in**
1461 **mitotic slippage-induced newly born tetraploid cells**
1462
1463 (**A)** Stills from time-lapse imaging of RPE-1 cells stably expressing mCherry-H2B after
1464 mitotic division (upper panel) or MS (lower panel). The nuclear contour during G1 is
1465 indicated, and the colour code shows the time spent in G1 (see methods). The pink
1466 arrow points at a nuclear deformation. **(B)** Left panel - Graph showing the nuclear
1467 circularity and solidity in G1 upon mitotic division (in grey, upper panel) or MS (in blue,
1468 lower panel). Right panel - Schematic representations of nuclear decondensation upon
1469 mitotic division (in grey, upper panel) or MS (in blue, lower panel). The data were
1470 measured in the cells presented in **(A**). **(C)** Representative images of diploid and MS-
1471 generated tetraploid RPE-1 G1 cells. Microtubules in cyan, DNA in magenta. The
1472 nuclear contour is indicated (yellow dotted line). **(D)** Graphs showing line scans
1473 measurements. **(E)** Left panel - Representative images showing diploid and MS-
1474 generated RPE-1 cells. Actin in grey, DNA in magenta. Right panel - Graphs showing
1475 line scan measurements. **(F)** Representative images showing microtubules (in cyan)
1476 in diploid and in EnR-generated RPE-1 cells. DNA in magenta. **(G)** Stills from time-
1477 lapse imaging of RPE-1 cells stably expressing mCherry-H2B (in magenta) performing
1478 MS. Actin was labelled using SPY650-FastAct (in grey). **(H)** Time-lapse still images
1479 from movies of RPE-1 cells stably expressing mCherry-H2B (in magenta undergoing
1480 MS. Microtubules in cyan. Scale bars: 10µm. D=diploid. T=tetraploid. MS=mitotic
1481 slippage. NEBD=nuclear envelope breakdown. A.U.=arbitrary unit.
1482

1483 **Figure S6: The microtubule cytoskeleton is the main contributor to nuclear**
1484 **deformations in tetraploid cells generated by mitotic slippage**
1485
1486 **(A)** Stills from time-lapse imaging of RPE-1 cells stably expressing mCherry-H2B (in
1487 magenta) undergoing MS and treated with DMSO (upper panel) or nocodazole (lower
1488 panel). Microtubules in cyan. **(B)** Graph presenting the delta circularity (defined as the
1489 difference between nuclear circularity in G2 vs in G1) in MS-generated tetraploid cells
1490 treated with DMSO or Nocodazole. Mean ± SEM, >90 cells analysed per condition,
1491 three independent experiments. **(C)** Graphs showing nuclear circularity (left panel) and
1492 solidity (right panel) in diploid and in MS-generated tetraploid RPE-1 cells (in grey and
1493 blue, respectively) treated with DMSO or with 2µM Nocodazole. Mean ± SEM, >105
1494 G1 cells analysed per condition, three independent experiments. **(D)** Graphs
1495 presenting the nuclear circularity and solidity from **(C)** in diploid and tetraploid G1 RPE-
1496 1 cells treated with DMSO or with Nocodazole. **(E)** Graphs showing nuclear circularity
1497 and solidity in diploid and in MS-generated tetraploid RPE-1 CCNB1 cells (in grey and
1498 blue, respectively) treated with DMSO or with 2µM Nocodazole. Mean ± SEM, >80 G1
1499 cells analysed per condition, three independent experiments. **(F)** Stills from time-lapse
1500 imaging of RPE-1 CCNB1 cells stably expressing mCherry-H2B (in magenta) treated
1501 with DMSO or Nocodazole and performing MS. **(G)** Graph showing the delta circularity
1502 (defined as the difference between nuclear circularity in G2 vs in G1) upon mitotic
1503 division (in grey) or MS (in blue) treated with DMSO (-) or Nocodazole. Mean ± SEM,
1504 >50 cells analysed per condition, three independent experiments. **(H)** Graphs
1505 displaying nuclear circularity and solidity indices in diploid and in MS-generated
1506 tetraploid RPE-1 cells (in grey and blue, respectively) treated with DMSO or Taxol.
1507 Mean ± SEM, >140 G1 cells analysed per condition, three independent experiments.
1508 **(I)** Graph presenting the nuclear circularity and solidity from **(H)** in diploid and tetraploid
1509 G1 RPE-1 cells treated with DMSO or with 1nM Taxol. Scale bars: 10µm. D=diploid.
1510 T=tetraploid. MS=mitotic slippage. CF=cytokinesis failure. EnR= endoreplication.
1511 A.U.=arbitrary unit. **(B)** t-test (two-sided). **(C,E,G,H)** Anova-test (one-sided). ns=not
1512 significant. *=P ≤ 0.05. **= P ≤ 0.01. ***= P ≤ 0.001. ****= P ≤ 0.0001.
1513
1514

Figure S7: Mitotic slippage promotes local changes in the Lamina network and in H3K9me2 levels

(A) Left panel – Graph showing the relative H3K9me2 mean intensity at the nuclear envelope in diploid (in grey) and tetraploid (in blue) G1 RPE-1 cells. Right panel – SIM representative images showing diploid and tetraploid G1 RPE-1 cells. H3K9me2 in cyan hot. Mean ± SEM, >90 G1 cells analysed per condition, three independent experiments. **(B)** Left panel – Graph showing the relative H3K9me2 mean intensity at the nuclear envelope in diploid (in grey) and tetraploid (in blue) G1 RPE-1 cells. Mean ± SEM, >90 G1 cells analysed per condition, three independent experiments. Right panel – SIM representative images showing diploid and tetraploid G1 RPE-1 cells. H3K9me2 in cyan hot. **(C)** Left panel – Graph showing the relative H3K9me2 mean intensity at the nuclear envelope in diploid (in grey) and tetraploid (in blue) G1 RPE-1 cells. Mean ± SEM, >90 G1 cells SIM resolution representative images showing diploid and tetraploid G1 RPE-1 cells. H3K9me2 in cyan hot. **(D)** Graph presenting the H3K9me2 coefficient of variation at the nuclear envelope in MS-induced tetraploid G1 RPE-1 cells. Mean ± SEM, >90 G1 cells analysed per condition, three independent experiments. **(E)** Graphs showing the relative H3K9me2 mean intensity (left panel) or the Lamin B1 vs A/C ratio (right panel) at the nuclear envelope in MS-induced tetraploid RPE-1 CCNB1 cells. Mean ± SEM, >90 G1 cells analysed per condition, three independent experiments. **(F-G)** Graphs of H3K9me2 mean intensity at the NE (left panel), H3K9me2 coefficient of variation at the NE (central panel) and Lamin A/C mean intensity at the NE (right panel) in diploid and in MS-generated tetraploid **(F)** BJ and **(G)** HCT116 cells. Mean ± SEM, >60 G1 cells analysed per condition, three independent experiments. **(H)** SIM representative images showing diploid and tetraploid cells generated by EnR or CF. H3K9me2, Lamin A/C and Lamin B1 in cyan hot, yellow hot and red hot, respectively. DNA in magenta. **(I)** Graphs showing the H3K9me2 coefficient of variation in diploid (in grey) and tetraploid G1 RPE-1 cells generated by EnR (in red) or CF (in yellow). Mean ± SEM, >90 G1 cells analysed per condition, three independent experiments. **(J)** Graphs showing the relative H3K9me3 (left panel) or H3K27me3 (right panel) mean intensity in diploid (in grey) and tetraploid (in blue) RPE-1 G1 cells. Mean ± SEM, >90 G1 cells analysed per condition, three independent experiments. **(K)** Graphs showing the relative H3K9ac (left panel) or H3K27ac (right panel) mean intensity in diploid (in grey) and tetraploid (in blue) RPE-1 G1 cells. Mean ± SEM, >90 G1 cells analysed per condition, three independent experiments. **(L)** Graphs presenting the relative mean intensity at the nuclear envelope of the indicated proteins in tetraploid RPE-1 G1 cells. Mean ± SEM, >90 G1 cells analysed per condition, at least three independent experiments. **(M)** Graphs showing the Lamin B1 vs A/C ratio (left panel) or the H3K9me2 mean intensity (right panel) at the nuclear envelope in diploid (in grey) and tetraploid (in blue) RPE-1 G1 cells treated with DMSO or with Nocodazole. Mean ± SEM, >90 G1 cells analysed per condition, three independent experiments. Scale bars: 10µm. D=diploid. T=tetraploid. MS=mitotic slippage. EnR=Endoreplication. CF=Cytokinesis failure. A.U.=arbitrary unit. **(M)**

Anova-test (one-sided). **(A,B,C,D,E,F,G,I,J,K,L)** t-test (two-sided). ns=not significant. *=P ≤ 0.05. **= P ≤ 0.01. ***= P ≤ 0.001. ****= P ≤ 0.0001.

1561 **Figure S8: Comparison of chromosome interactions and gene expression in**
1562 **tetraploid and diploid RPE1 cells**
1563
1564 **(A)** Scheme presenting the experimental workflow used to isolate diploid and tetraploid
1565 cells. **(B)** Graph showing the percentage of G1 diploid (in grey) and MS-generated
1566 tetraploid (in blue) RPE-1 cells before and after cell sorting. Mean ± SEM, >900 cells
1567 analysed, five independent experiments. **(C)** Representative images showing diploid
1568 and MS-generated tetraploid cells after cell sorting. DNA in magenta. **(D-E)** Boundary
1569 insulation scores for **(D)** all and **(E)** top 300 most strongly insulating boundaries
1570 between diploid (x-axis) and tetraploid (y-axis) conditions. **(F)** Relationship between
1571 observed and expected intra-chromosomal values in tetraploid versus diploid. Each
1572 dot represents an inter-chromosomal interaction, red signifies higher and blue lower
1573 interaction signal in tetraploid compared to control. **(G)** Remodeling of interactions
1574 between chromatin sub-compartments in tetraploid and diploid cells. Blue suggests a
1575 loss of interaction, red a gain of interactions. **(H)** Volcano plot of RNAseq data obtained
1576 by comparing gene expression in tetraploid G1 cells generated by MS with diploid G1
1577 cells. D=diploid. T=tetraploid. MS=mitotic slippage. ns=not significant. **(D,E,F,G)** two-
1578 tailed Wilcoxon test. *=P ≤ 0.05. **= P ≤ 0.01. ***= P ≤ 0.001. ****= P ≤ 0.0001.
1579

1580 **Figure S9: Physiological polyploid cells generated by cytokinesis failure and**
1581 **endoreplication show homogenous nuclear shape**
1582
1583 **(A)** Representative images of small and large MKs. DNA in magenta. **(B)** Graph
1584 showing nuclear area in diploid progenitors and in polyploid MKs. The MK median
1585 nuclear area was used to distinguish small and large MKs. Mean ± SEM, >150
1586 interphase cells analysed per condition, three independent experiments. **(C)**
1587 Schematic workflow showing the methods used to obtain mouse hepatocytes. **(D)**
1588 Representative images showing diploid and polyploid hepatocytes. Actin in grey, DNA
1589 in magenta. **(E)** SIM representative images and their corresponding 3D reconstructions
1590 showing diploid and polyploid hepatocytes. Lamin A/C in yellow, DNA in magenta. **(F)**
1591 Schematic representation of *Drosophila* salivary glands. **(G)** Representative images
1592 and their corresponding 3D reconstructions showing polyploid salivary glands. Lamin
1593 A/C in yellow, DNA in magenta. **(H)** Left panel - Graph showing the nuclear area in
1594 diploid and in polyploid hepatocytes (in grey and yellow, respectively). The hepatocyte
1595 median nuclear area was used to distinguish small and large hepatocytes.
1596 Mean ± SEM, >140 interphase cells analysed per condition, three independent
1597 experiments. Right panel – Representative images showing diploid and polyploid
1598 hepatocytes. DNA in magenta. **(I)** Graph showing the nuclear area and in polyploid
1599 salivary glands at two different developmental stages (L2 and L3). Mean ± SEM, >100
1600 cells analysed, three independent experiments. **(J)** Representative
1601 immunofluorescence images showing *Drosophila* fat body (left panel) and ring gland
1602 (right panel). Lamin A/C or Nuclear pore complex (NPC) in yellow hot, Actin in grey,
1603 DNA in magenta. Scale bars: 10µm. D=diploid. P=polyploid. MK=megakaryocyte.
1604 NPC=Nuclear pore complex. **(B,H,I)** t-test (two-sided). ns=not significant. *=P ≤ 0.05.
1605 **= P ≤ 0.01. ***= P ≤ 0.001. ****= P ≤ 0.0001.
1606

Figure S10: Polyploid hepatocytes and salivary gland cells do no show defects in H3K9me2 and Lamin A/C distribution

(A-D) Graphs showing **(A)** H3K27ac, **(B)** H3K9me3 and **(C)** H3K9me2 mean intensity in the nucleus in diploid progenitors (in grey) and in polyploid megakaryocytes (in blue). Mean ± SEM, >120 cells analysed, three independent experiments and Lamin B1 mean intensity at the nuclear envelope **(D)**in diploid progenitors (in grey) and in polyploid megakaryocytes (in blue). **(E)** SIM representative images of diploid progenitors and polyploid megakaryocyte. H3K9me2 in cyan hot, DNA in magenta. **(F-G)** Graphs showing H3K9me2 **(F)** mean intensity and **(G**) coefficient of variation (define as the ratio of the standard deviation to the mean) in progenitors (in grey) and in MKs (in blue). Mean ± SEM, >150 interphase cells analysed per condition, four independent experiments. **(H)** Graph showing H3K9me2 mean intensity in progenitors (in grey) and in MKs (in blue). Mean ± SEM, >65 interphase cells analysed per condition, four independent experiments. **(I)** Representative images of microtubules (in cyan) in MKs, DNA in magenta. **(J)** SIM representative images showing diploid and polyploid hepatocytes. Lamin A/C, Lamin B1 and H3K9me2 in yellow hot, red hot and cyan hot, respectively, DNA in magenta. **(K-L)** Graphs showing **(K)** the relative H3K9me2 mean intensity at the NE and **(L)** the H3K9me2 coefficient of variation (define as the ratio of the standard deviation to the mean) at the NE in diploid (in grey) and in polyploid (in yellow) hepatocytes. Mean ± SEM, >90 interphase cells analysed per condition, three independent experiments. **(M-O)** Graphs presenting **(M)** Lamin A/C and **(N**) Lamin B1 mean intensity at the NE and **(O)** the Lamin B1 vs Lamin A/C ratio at the NE in hepatocytes. Mean ± SEM, >90 interphase cells analysed per condition, three independent experiments. **(P)** Representative images showing *Drosophila* salivary glands at two different developmental stages (L2 and L3). Lamin A/C and Lamin B1 in yellow hot and red hot, respectively, Actin in grey, DNA in magenta. **(Q-R)** Graphs showing **(Q)** Lamin A/C and **(R)** Lamin B1 mean intensity at the NE in *Drosophila* salivary glands. Mean ± SEM, >150 cells analysed per condition, three independent experiments. **(S)** Representative images showing (left panel) polyploid hepatocytes and (right panel) *Drosophila* salivary gland cells. Microtubules in cyan. DNA in magenta. **(T)** Graph presenting the nuclear circularity and solidity index in progenitors (in grey) or megakaryocytes (in blue) treated with DMSO or Nocodazole. Scale bars: 10µm. D=diploid. P=polyploid. HC=hepatocytes. MK=megakaryocytes. NE=nuclear envelope. **(D)** Anova-test (one-sided). **(F,G,J,K,L,M,N,P)** t-test (two-sided). ns=not significant. *=P ≤ 0.05. **= P ≤ 0.01. ***= P ≤ 0.001. ****= P ≤ 0.0001.

Videos 1 and 2: Mitotic slippage generates tetraploid cells with nuclear deformations.
Time lapse videos of RPE-1 cells expressing mCherry-H2B (in magenta) and performing canonical mitosis (video 1) or mitotic slippage (video 2). Images were acquired every 5 minutes.

Videos 3 and 4: Microtubules accumulate around nuclear deformations upon mitotic slippage.
Time lapse videos of RPE-1 cells expressing mCherry-H2B (in magenta) performing mitotic slippage. Microtubules were labeled using SPY Tubulin (in Cyan, video 3) and actin was labeled using SPY FAST Actin (in blue, video 4). Images were acquired every 3 minutes.

Videos 5 and 6: Microtubule depolymerization prevents nuclear deformations upon mitotic slippage.
Time lapse videos of RPE-1 cells expressing mCherry-H2B (in magenta) and performing mitotic slippage in the absence (video 5) or presence of Nocodazole (video 6). Microtubules were labeled using SPY Tubulin (in Cyan). Images were acquired every 3 minutes.

Videos 7 and 8: Microtubule depolymerization prevents nuclear deformations upon mitotic slippage induced by CCNB1 depletion.
Time lapse videos of RPE-1 CCNB1 cells expressing mCherry-H2B (in magenta) and performing mitotic slippage in the absence (video 7) or presence of Nocodazole (video 8). Microtubules were labeled using SPY Tubulin (in Cyan). Images were acquired every 3 minutes.

Videos 9 and 10: Megakaryocytes become polyploid by mitotic slippage.
Time lapse videos Megakaryocytes expressing mCherry-H2B (in magenta) and performing mitotic slippage. Images were acquired every 10 minutes.

Figure 1

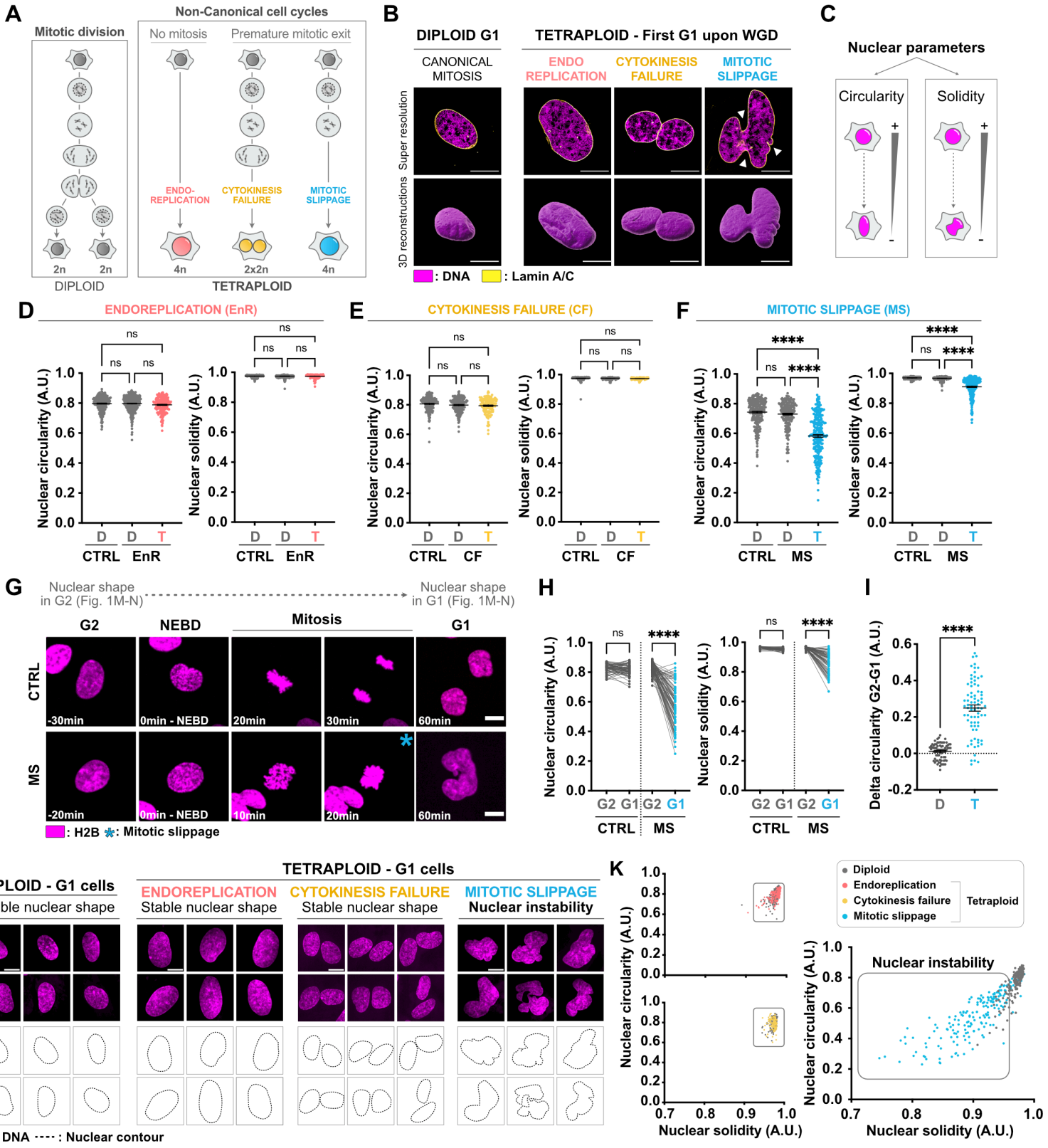
A
Mitotic division
Non-Canonical cell cycles
No mitosis
Premature mitotic exit
ENDO-REPLICATION
CYTOKINESIS FAILURE
MITOTIC SLIPPAGE
2n
2n
4n
2x2n
4n
DIPLOID
TETRAPLOID
B
DIPLOID G1
TETRAPLOID - First G1 upon WGD
CANONICAL MITOSIS
ENDO REPLICATION
CYTOKINESIS FAILURE
MITOTIC SLIPPAGE
Super resolution
3D reconstructions
: DNA
: Lamin A/C
C
Nuclear parameters
Circularity
Solidity
D
ENDOREPLICATION (EnR)
E
CYTOKINESIS FAILURE (CF)
F
MITOTIC SLIPPAGE (MS)
Nuclear circularity (A.U.)
Nuclear solidity (A.U.)
CTRL
EnR
CF
MS
G
Nuclear shape in G2 (Fig. 1M-N)
Nuclear shape in G1 (Fig. 1M-N)
G2
NEBD
Mitosis
G1
CTRL
MS
-30min
0min - NEBD
20min
30min
60min
-20min
10min
: H2B
: Mitotic slippage
H
I
Delta circularity G2-G1 (A.U.)
J
DIPLOID - G1 cells
Stable nuclear shape
TETRAPLOID - G1 cells
ENDOREPLICATION
Stable nuclear shape
CYTOKINESIS FAILURE
Stable nuclear shape
MITOTIC SLIPPAGE
Nuclear instability
: DNA
: Nuclear contour
K
Diploid
Endoreplication
Cytokinesis failure
Mitotic slippage
Tetraploid
Nuclear instability
Nuclear solidity (A.U.)

Figure 2

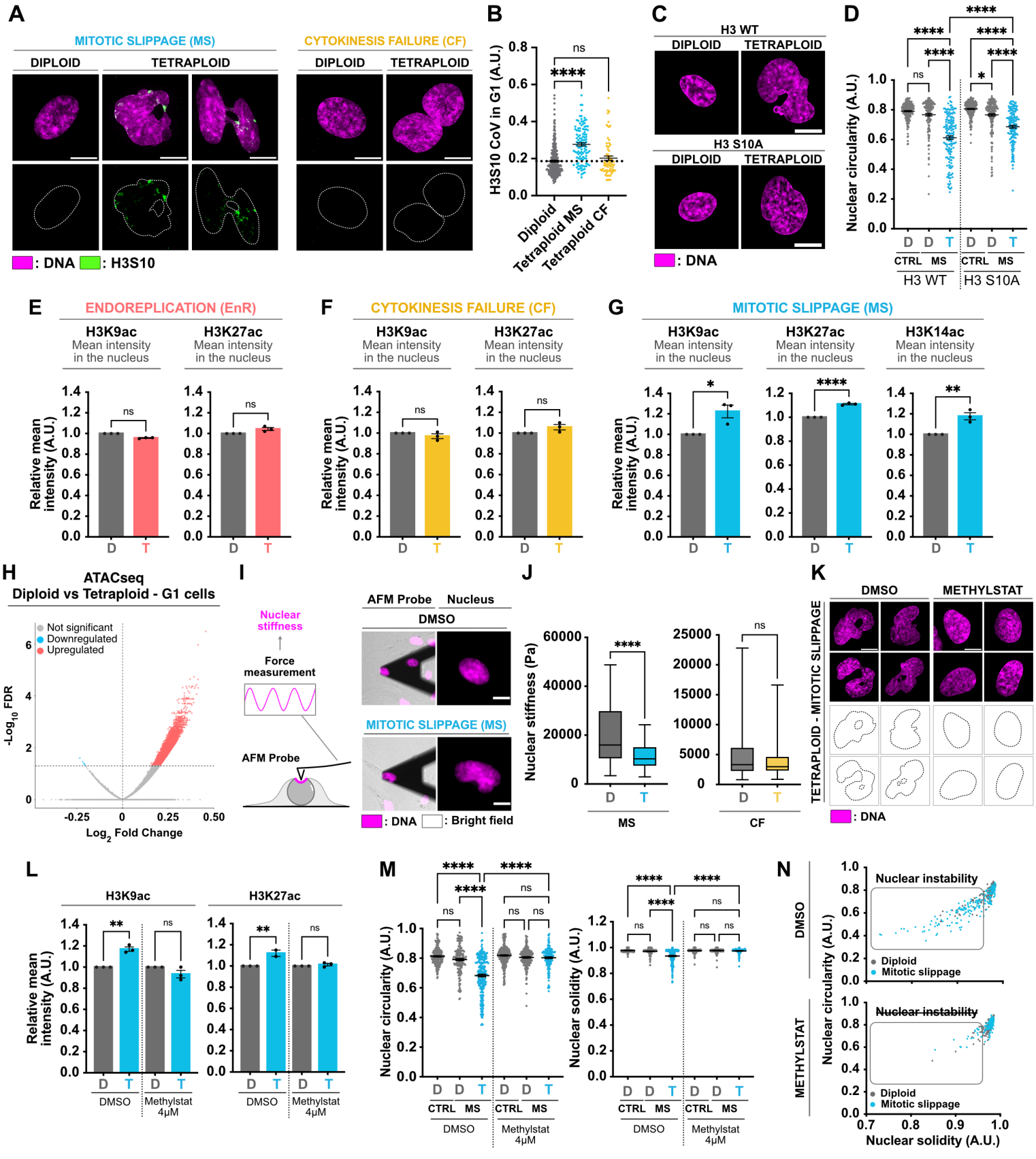
A
MITOTIC SLIPPAGE (MS)
CYTOKINESIS FAILURE (CF)
DIPLOID
TETRAPLOID
: DNA
: H3S10
B
H3S10 CoV in G1 (A.U.)
ns
****
Diploid
Tetraploid MS
Tetraploid CF
C
H3 WT
H3 S10A
DIPLOID
TETRAPLOID
: DNA
D
Nuclear circularity (A.U.)
CTRL
MS
H3 WT
H3 S10A
E
ENDOREPLICATION (EnR)
H3K9ac
H3K27ac
Mean intensity in the nucleus
Relative mean intensity (A.U.)
F
CYTOKINESIS FAILURE (CF)
G
MITOTIC SLIPPAGE (MS)
H3K14ac
H
ATACseq
Diploid vs Tetraploid - G1 cells
Not significant
Downregulated
Upregulated
-Log10 FDR
Log2 Fold Change
I
Nuclear stiffness
Force measurement
AFM Probe
J
Nuclear stiffness (Pa)
MS
CF
K
DMSO
METHYLSTAT
TETRAPLOID - MITOTIC SLIPPAGE
: DNA
L
Methylstat 4μM
M
Nuclear circularity (A.U.)
Nuclear solidity (A.U.)
N
Nuclear instability
Diploid
Mitotic slippage
Nuclear solidity (A.U.)

Figure 3

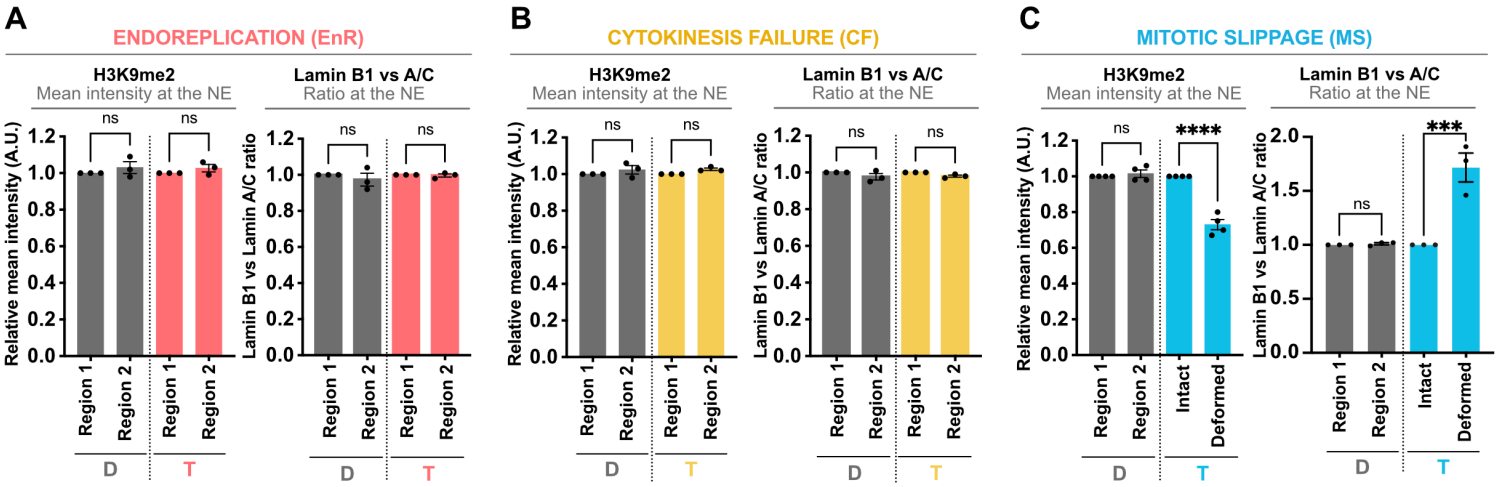
A
ENDOREPLICATION (EnR)
H3K9me2
Mean intensity at the NE
Lamin B1 vs A/C
Ratio at the NE
Relative mean intensity (A.U.)
Lamin B1 vs Lamin A/C ratio
ns
Region 1
Region 2
D
T
B
CYTOKINESIS FAILURE (CF)
C
MITOTIC SLIPPAGE (MS)
Intact
Deformed
****
***

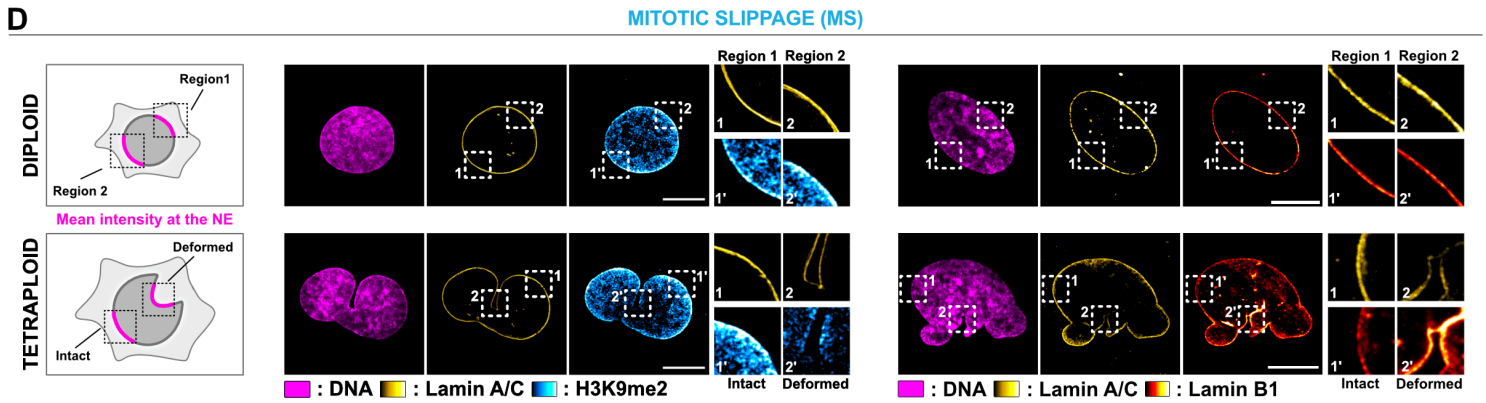
D
MITOTIC SLIPPAGE (MS)
DIPLOID
TETRAPLOID
Region1
Region 2
Mean intensity at the NE
Deformed
Intact
: DNA
: Lamin A/C
: H3K9me2
: Lamin B1

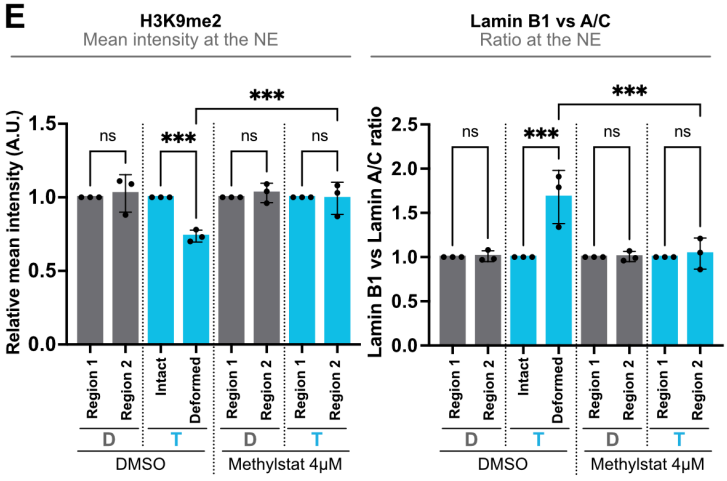
E
H3K9me2
Mean intensity at the NE
Lamin B1 vs A/C
Ratio at the NE
Relative mean intensity (A.U.)
Lamin B1 vs Lamin A/C ratio
ns
***
Region 1
Region 2
Intact
Deformed
D
T
DMSO
Methylstat 4μM

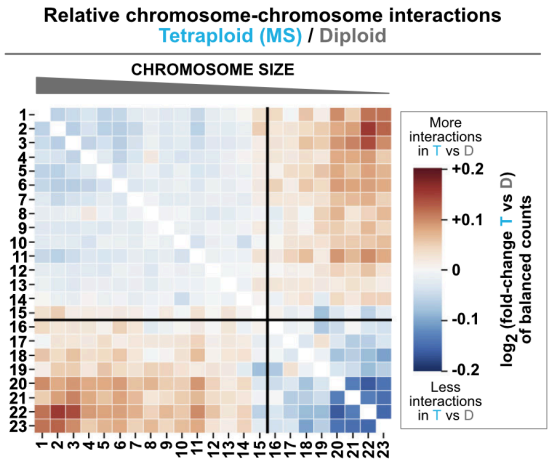
F
Relative chromosome-chromosome interactions
Tetraploid (MS) / Diploid
CHROMOSOME SIZE
More interactions in T vs D
Less interactions in T vs D
log2 (fold-change T vs D) of balanced counts
+0.2
+0.1
0
-0.1
-0.2

Figure 4

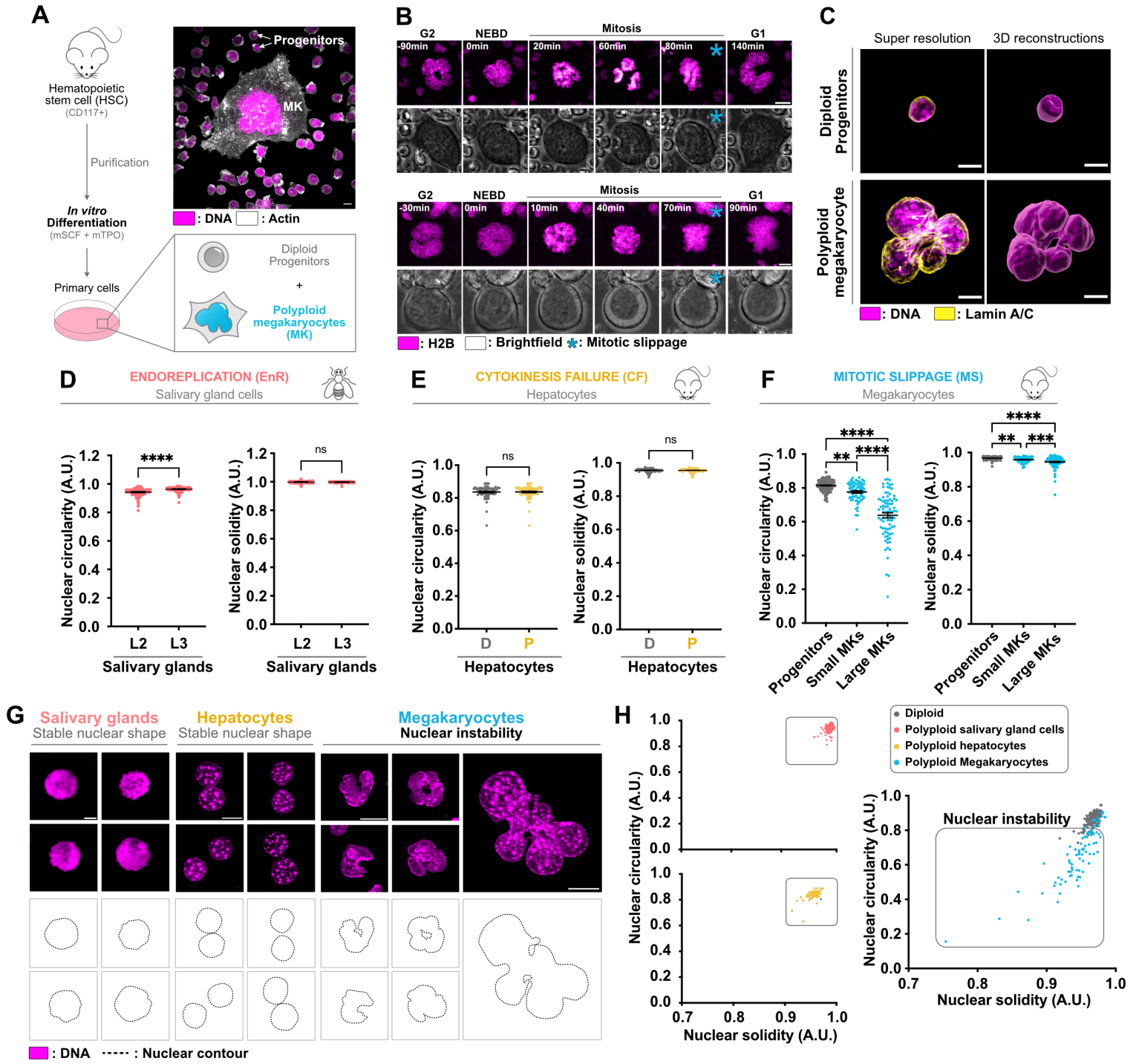
A
Hematopoietic stem cell (HSC)
(CD117+)
Purification
In vitro Differentiation
(mSCF + mTPO)
Primary cells
Progenitors
MK
: DNA : Actin
Diploid Progenitors
+
Polyploid megakaryocytes (MK)
B
G2
NEBD
Mitosis
G1
-90min
0min
20min
60min
80min
140min
-30min
10min
40min
70min
90min
: H2B : Brightfield : Mitotic slippage
C
Super resolution
3D reconstructions
Diploid Progenitors
Polyploid megakaryocyte
: DNA : Lamin A/C
D
ENDOREPLICATION (EnR)
Salivary gland cells
Nuclear circularity (A.U.)
Nuclear solidity (A.U.)
****
ns
L2
L3
Salivary glands
E
CYTOKINESIS FAILURE (CF)
Hepatocytes
D
P
F
MITOTIC SLIPPAGE (MS)
Megakaryocytes
**
***
Progenitors
Small MKs
Large MKs
G
Salivary glands
Stable nuclear shape
Hepatocytes
Stable nuclear shape
Megakaryocytes
Nuclear instability
: DNA ----- : Nuclear contour
H
Diploid
Polyploid salivary gland cells
Polyploid hepatocytes
Polyploid Megakaryocytes
Nuclear instability
Nuclear circularity (A.U.)
Nuclear solidity (A.U.)

Figure 5

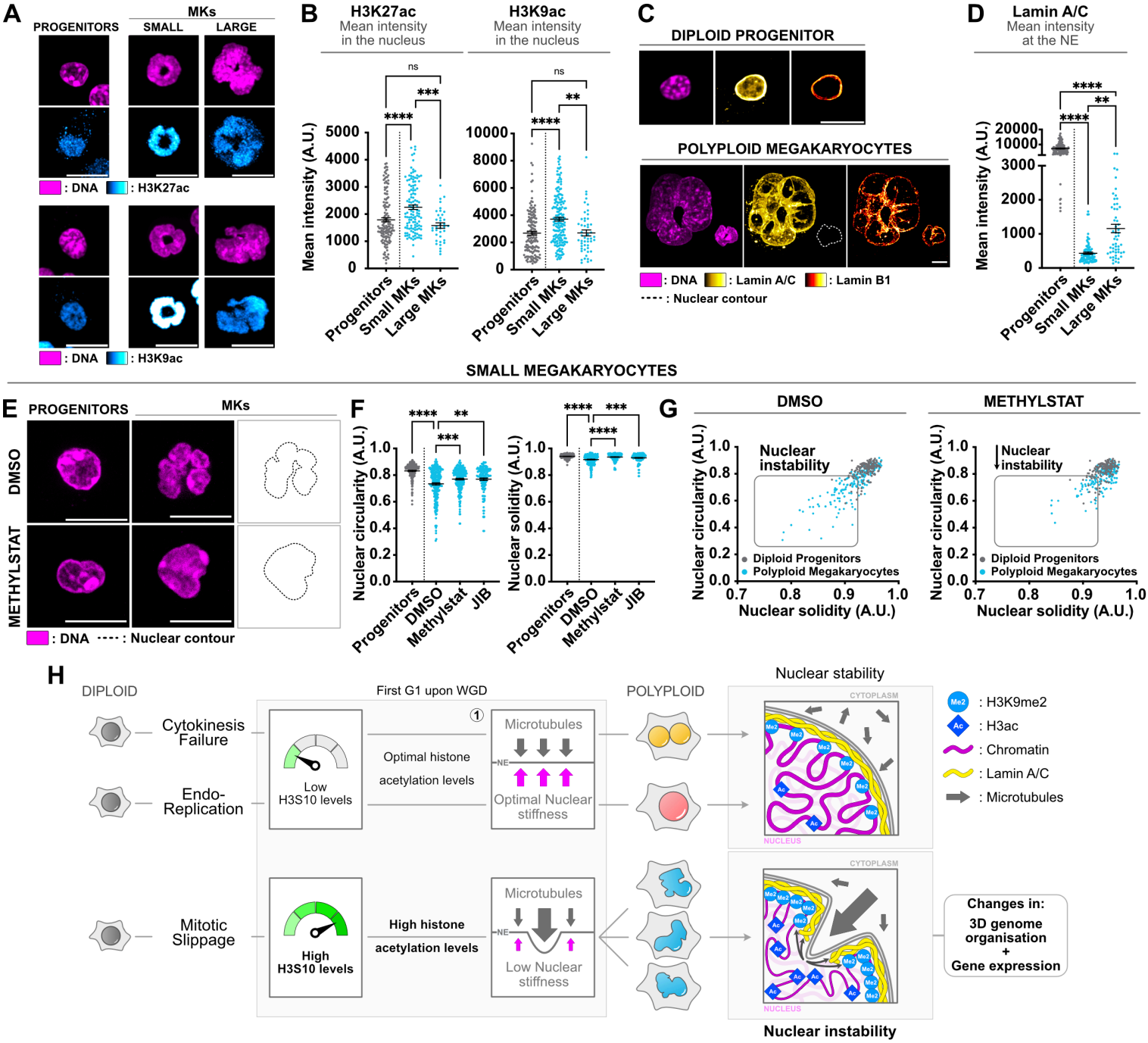
A
PROGENITORS
MKs
SMALL
LARGE
: DNA
: H3K27ac
: DNA
: H3K9ac
B
H3K27ac
Mean intensity in the nucleus
H3K9ac
Mean intensity in the nucleus
Mean intensity (A.U.)
ns
****
***
**
Progenitors
Small MKs
Large MKs
C
DIPLOID PROGENITOR
POLYPLOID MEGAKARYOCYTES
: DNA
: Lamin A/C
: Lamin B1
: Nuclear contour
D
Lamin A/C
Mean intensity at the NE
SMALL MEGAKARYOCYTES
E
PROGENITORS
MKs
DMSO
METHYLSTAT
: DNA
: Nuclear contour
F
Nuclear circularity (A.U.)
Nuclear solidity (A.U.)
Progenitors
DMSO
Methylstat
JIB
G
DMSO
METHYLSTAT
Nuclear instability
Diploid Progenitors
Polyploid Megakaryocytes
Nuclear solidity (A.U.)
Nuclear circularity (A.U.)
H
DIPLOID
Cytokinesis Failure
Endo-Replication
Mitotic Slippage
First G1 upon WGD
Low H3S10 levels
High H3S10 levels
Optimal histone acetylation levels
High histone acetylation levels
Microtubules
NE
Optimal Nuclear stiffness
Low Nuclear stiffness
POLYPLOID
Nuclear stability
CYTOPLASM
NUCLEUS
Nuclear instability
: H3K9me2
: H3ac
: Chromatin
: Lamin A/C
: Microtubules
Changes in:
3D genome organisation
+
Gene expression

Supp Figure 1

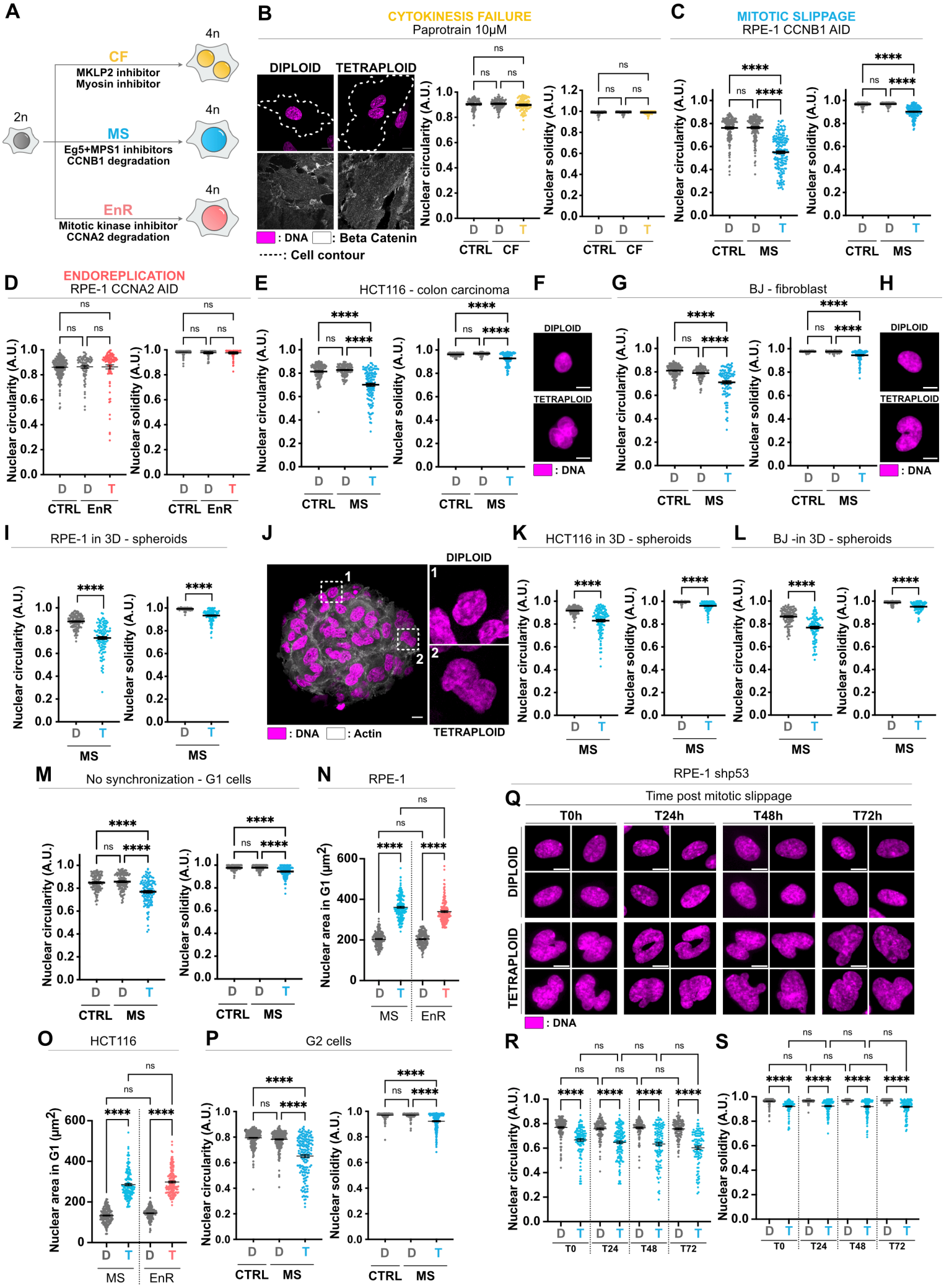

Supp Figure 2

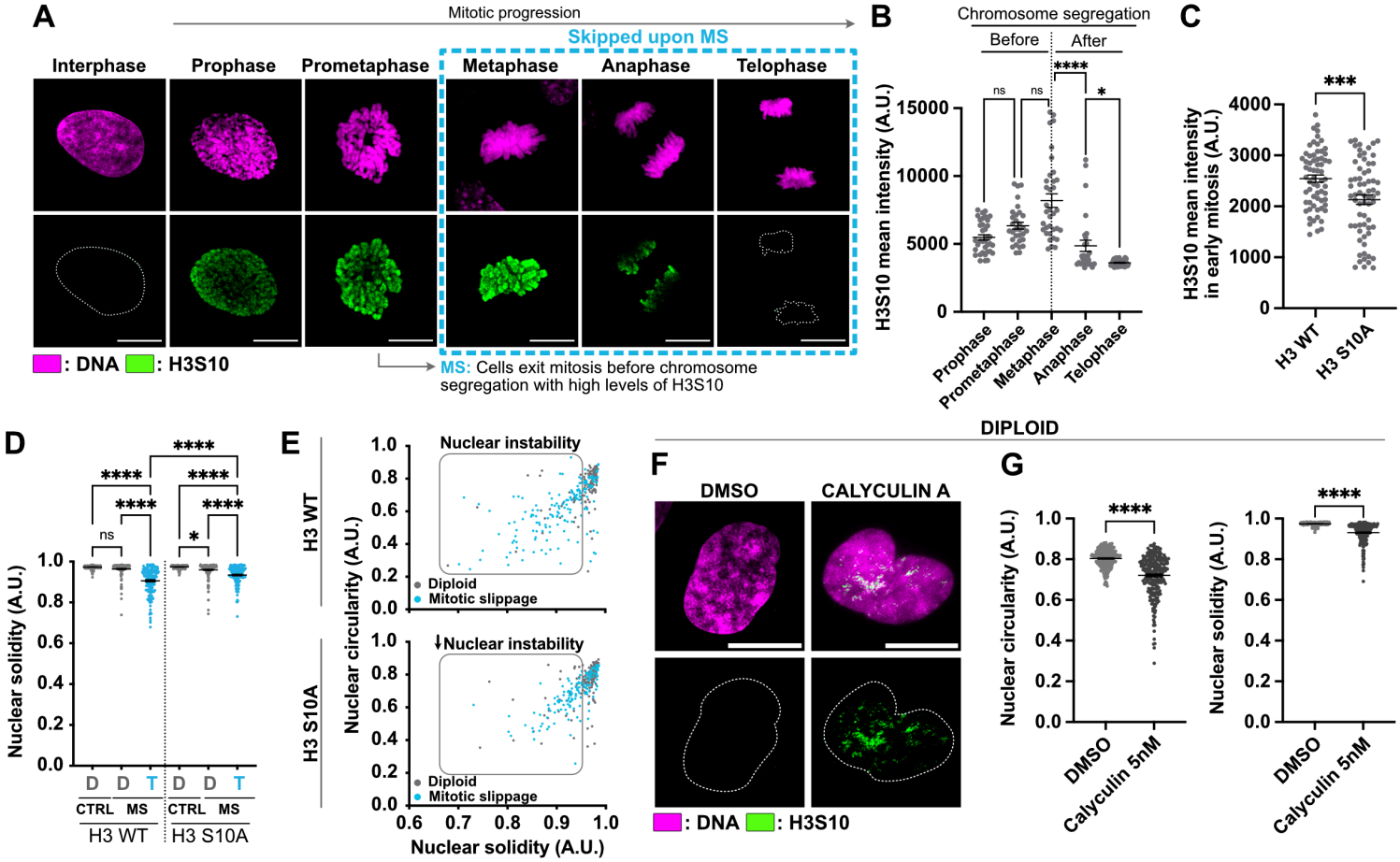

Supp Figure 3

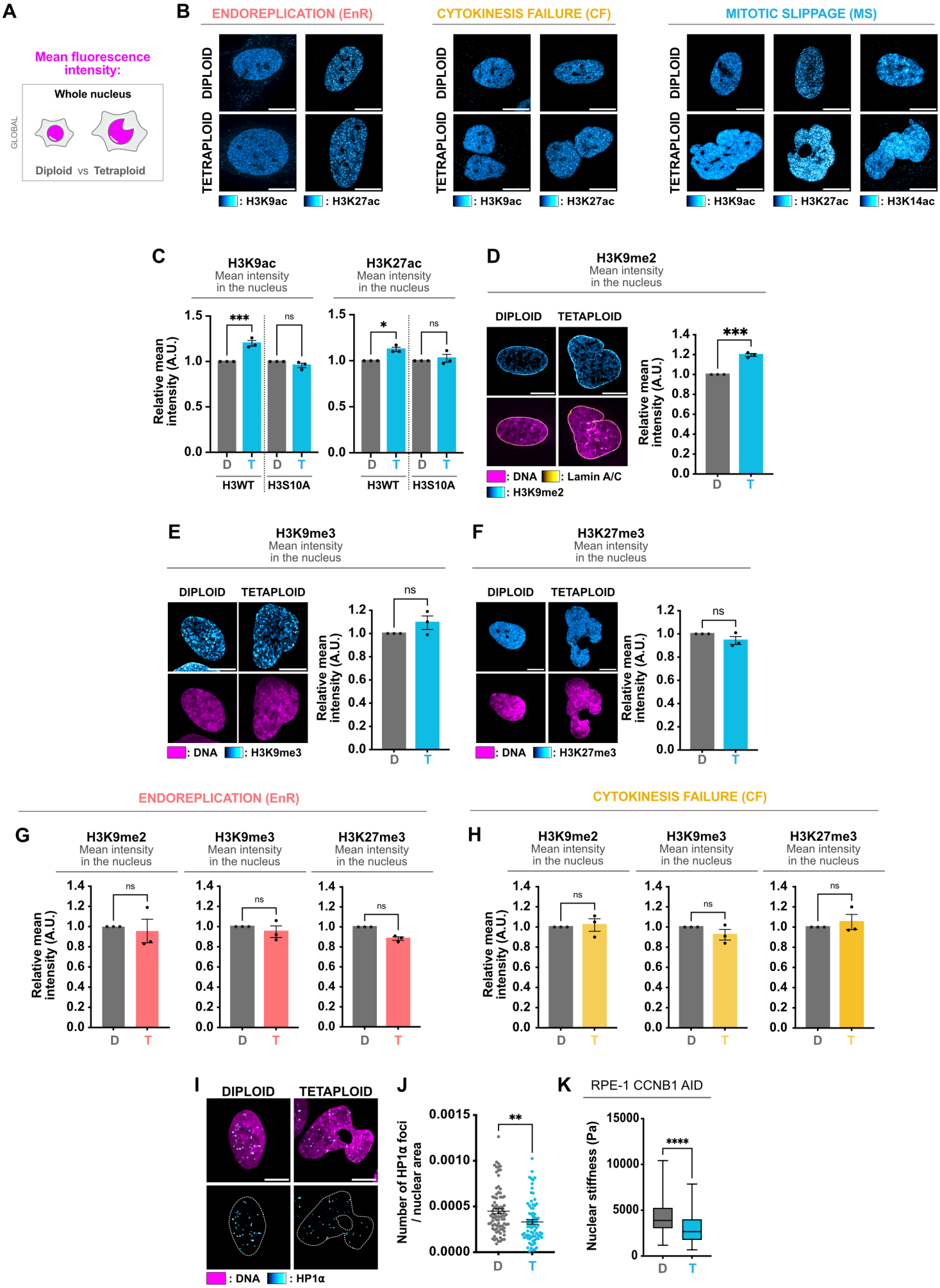

Supp Figure 4

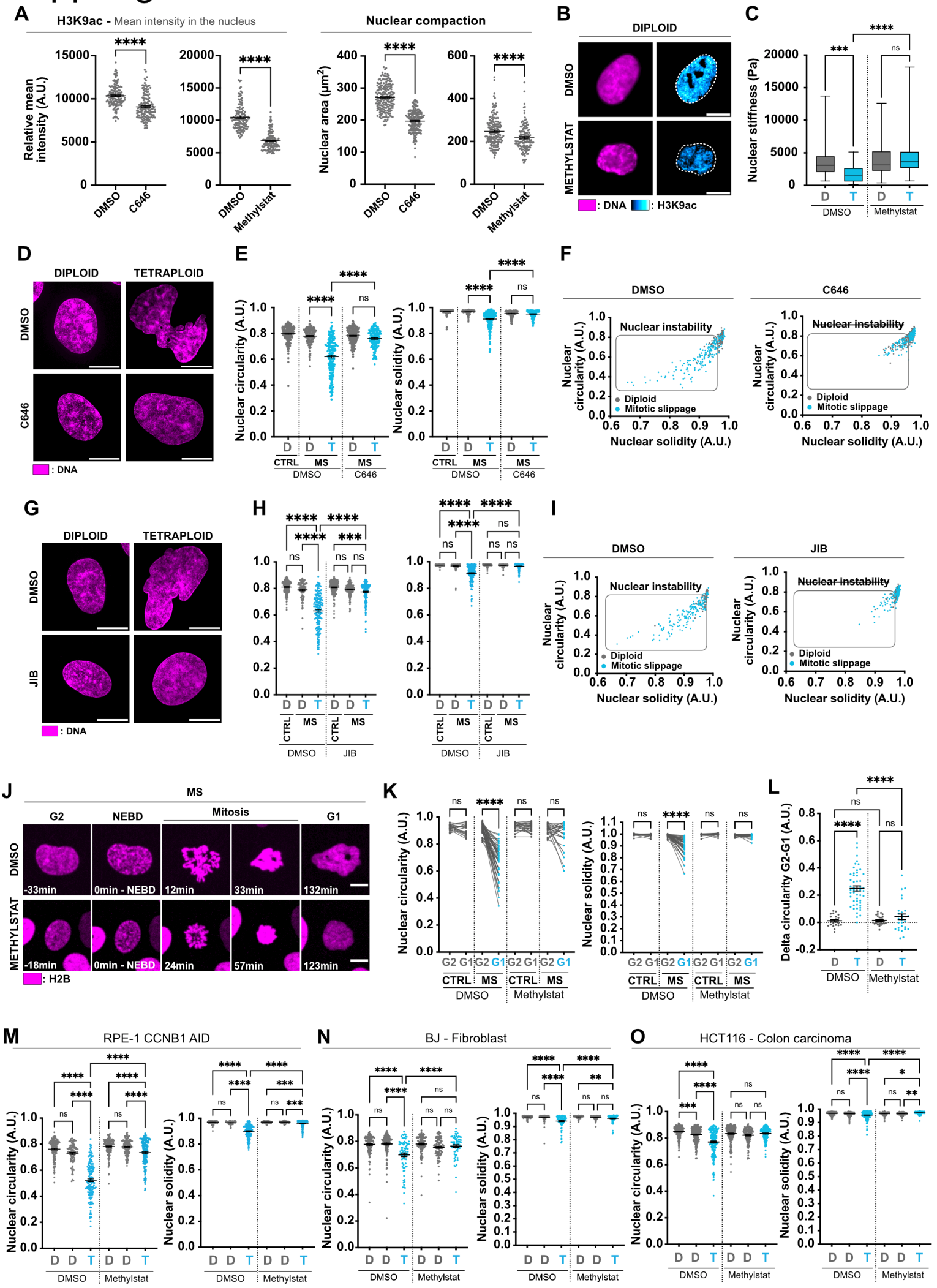

Supp Figure 5

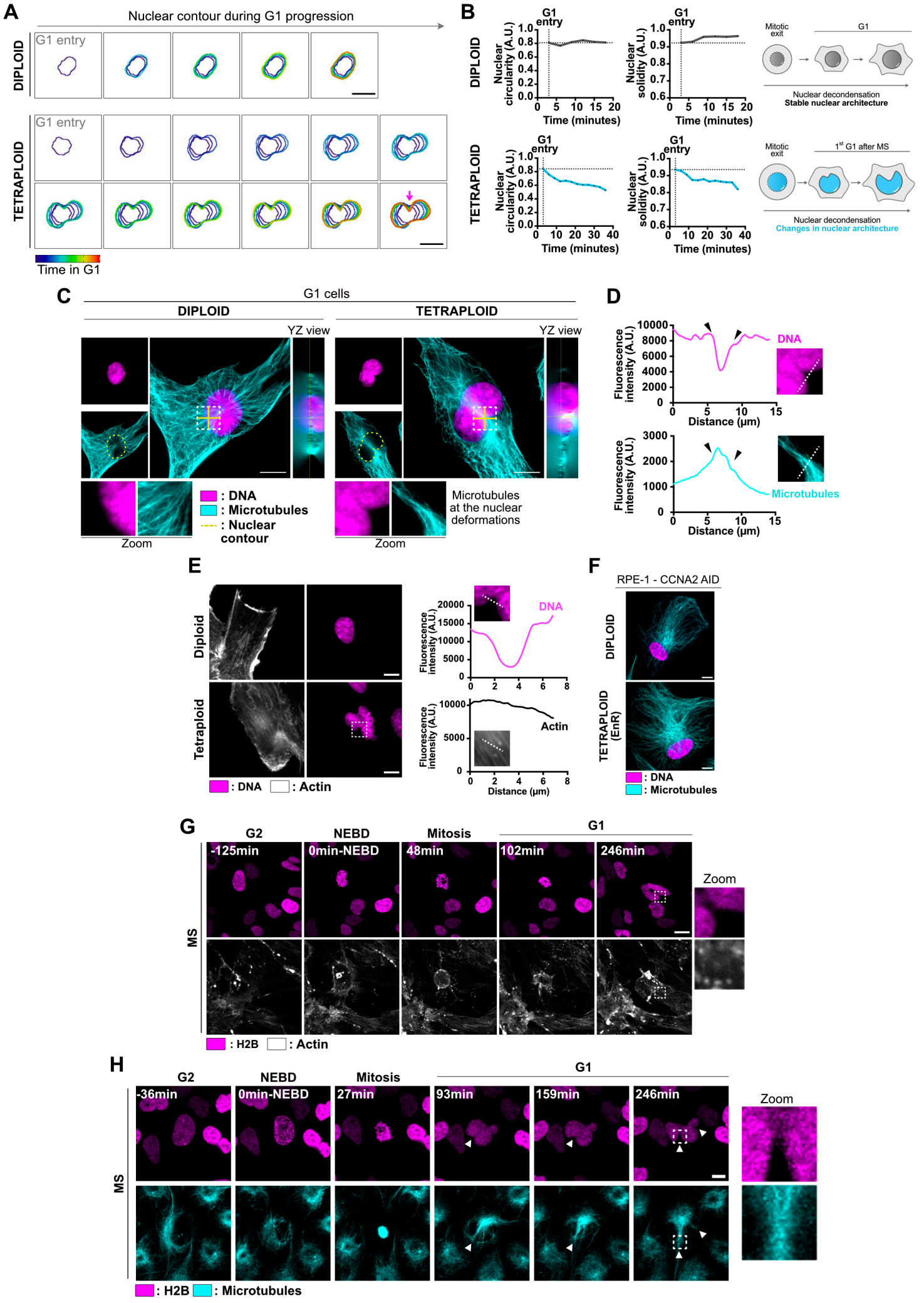

Supp Figure 6

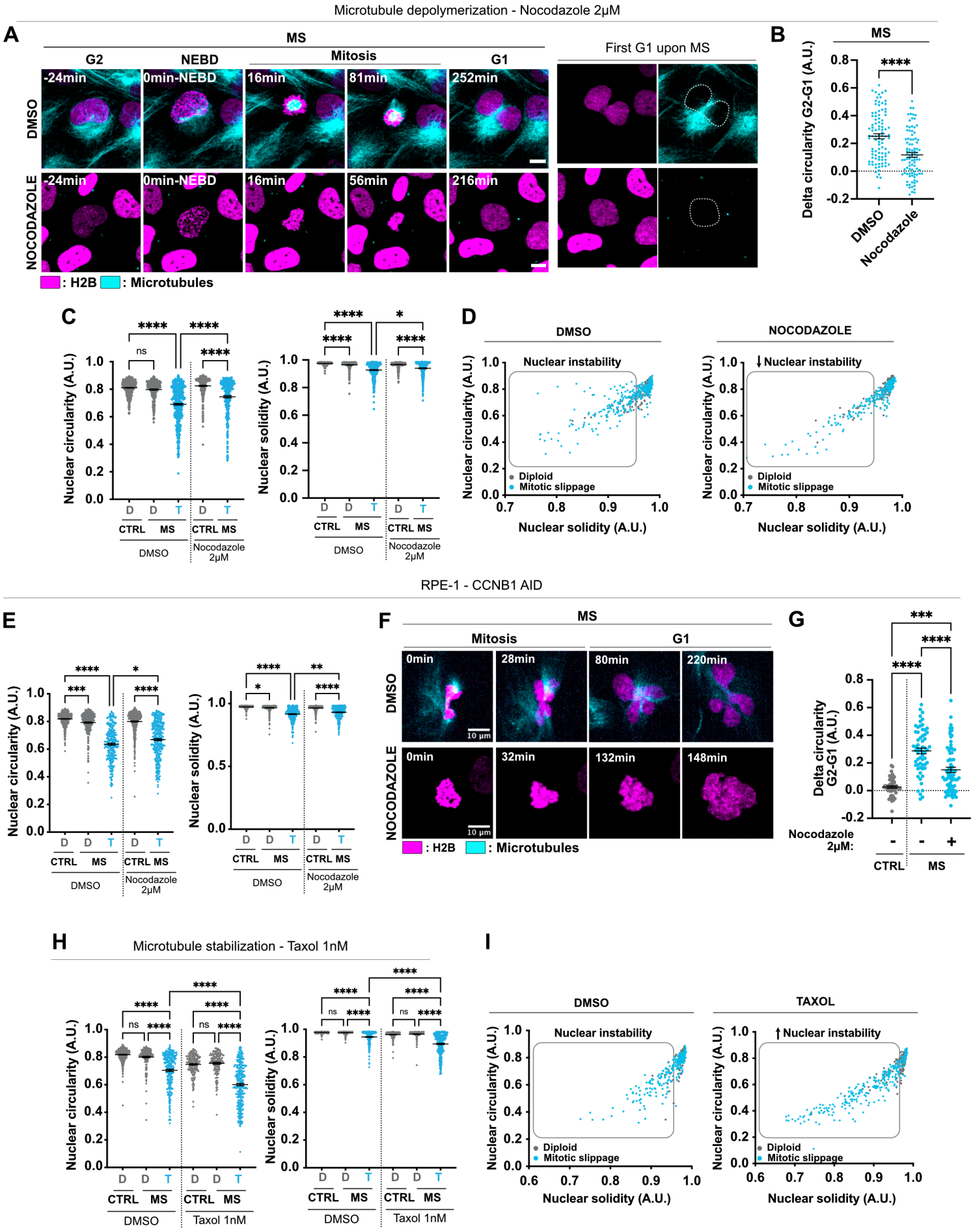

Supp Figure 7

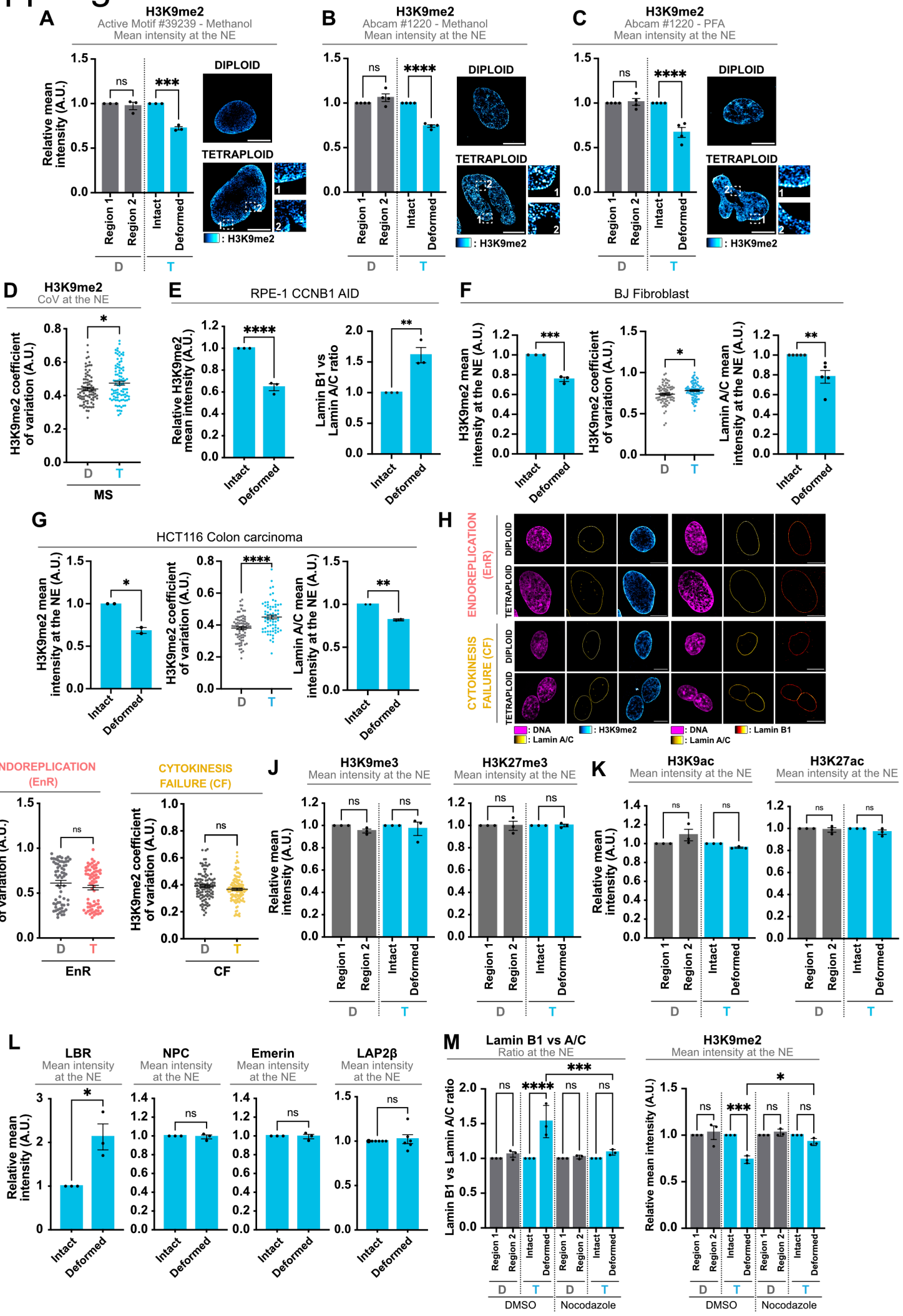

Supp Figure 8

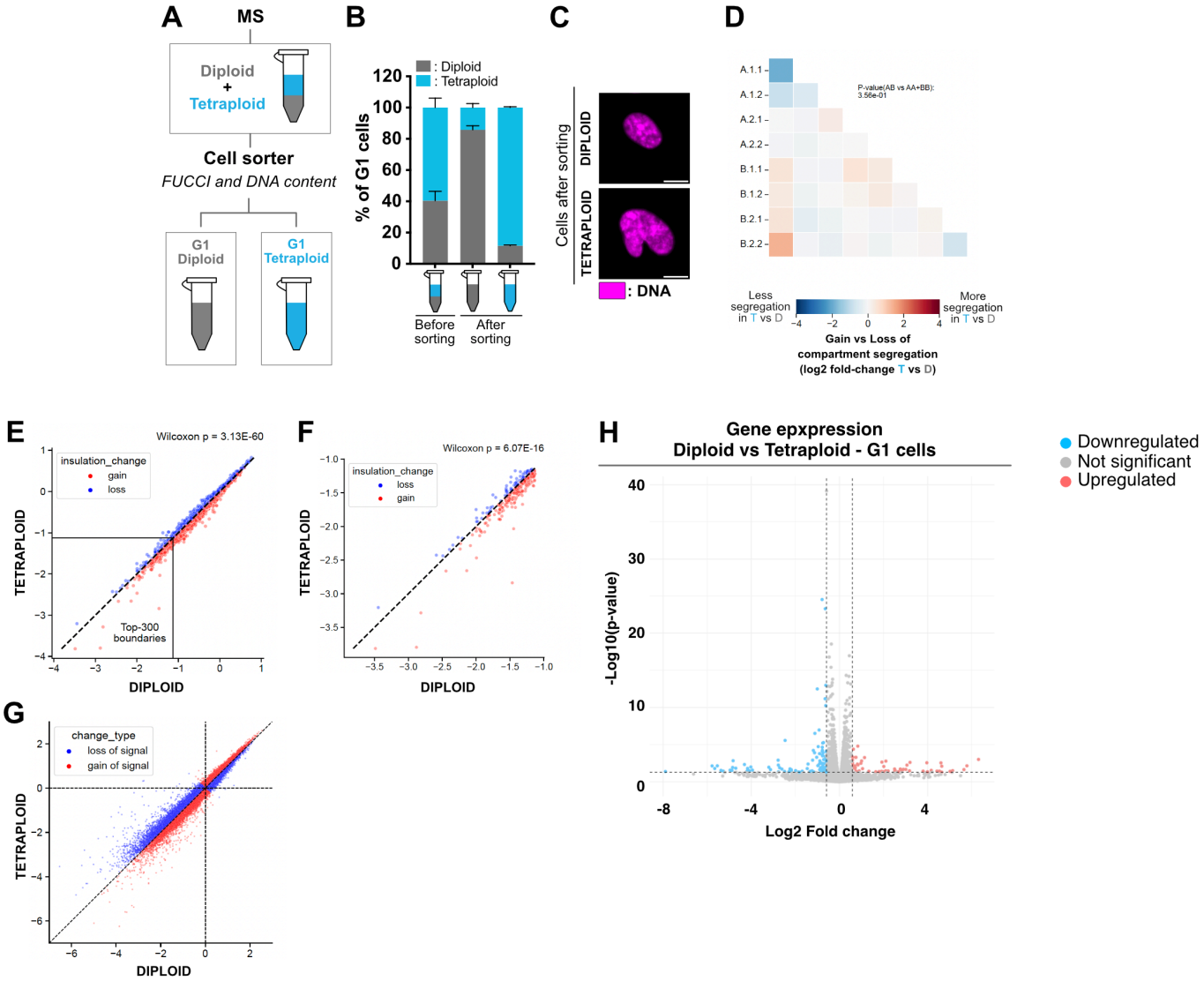

Supp Figure 9

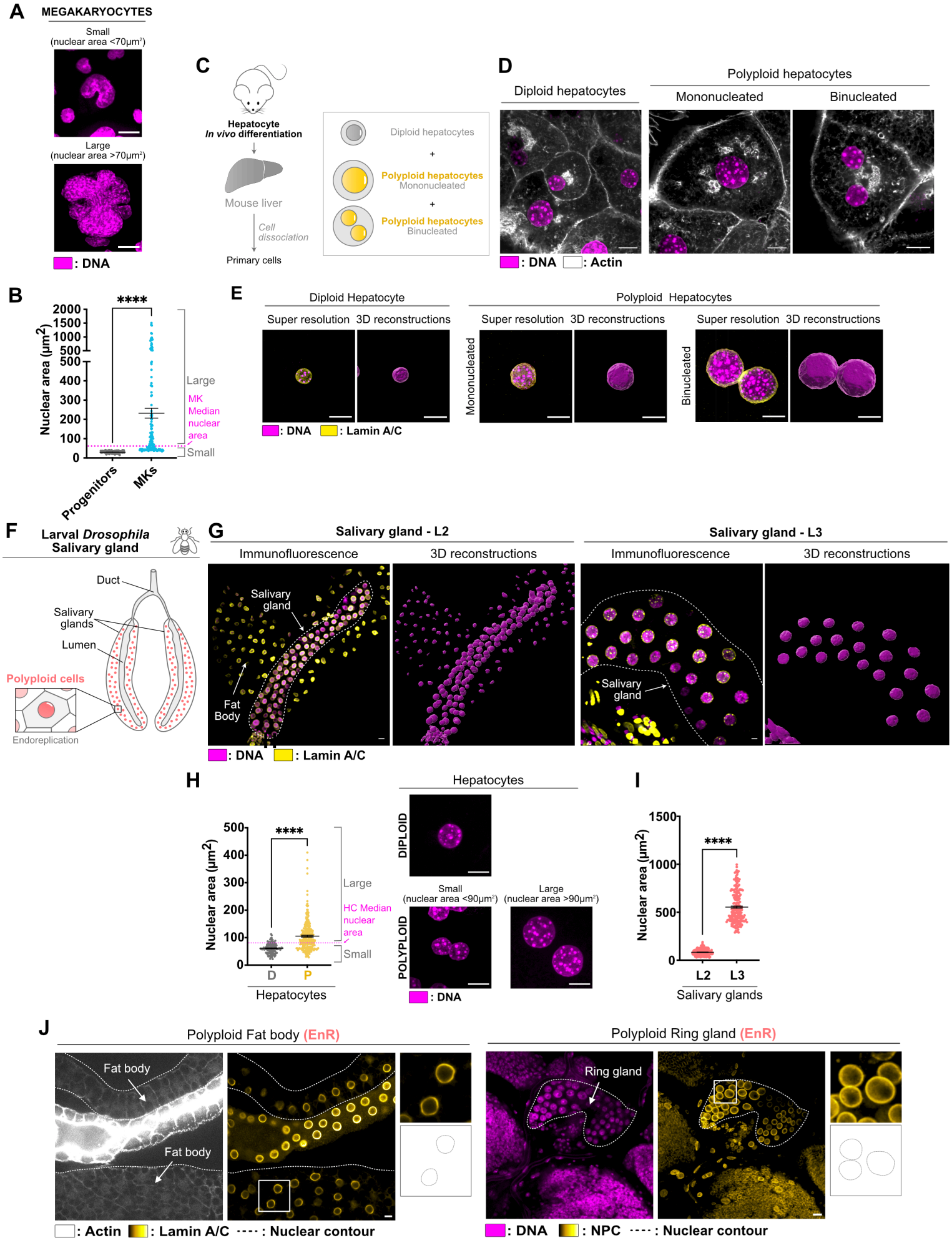
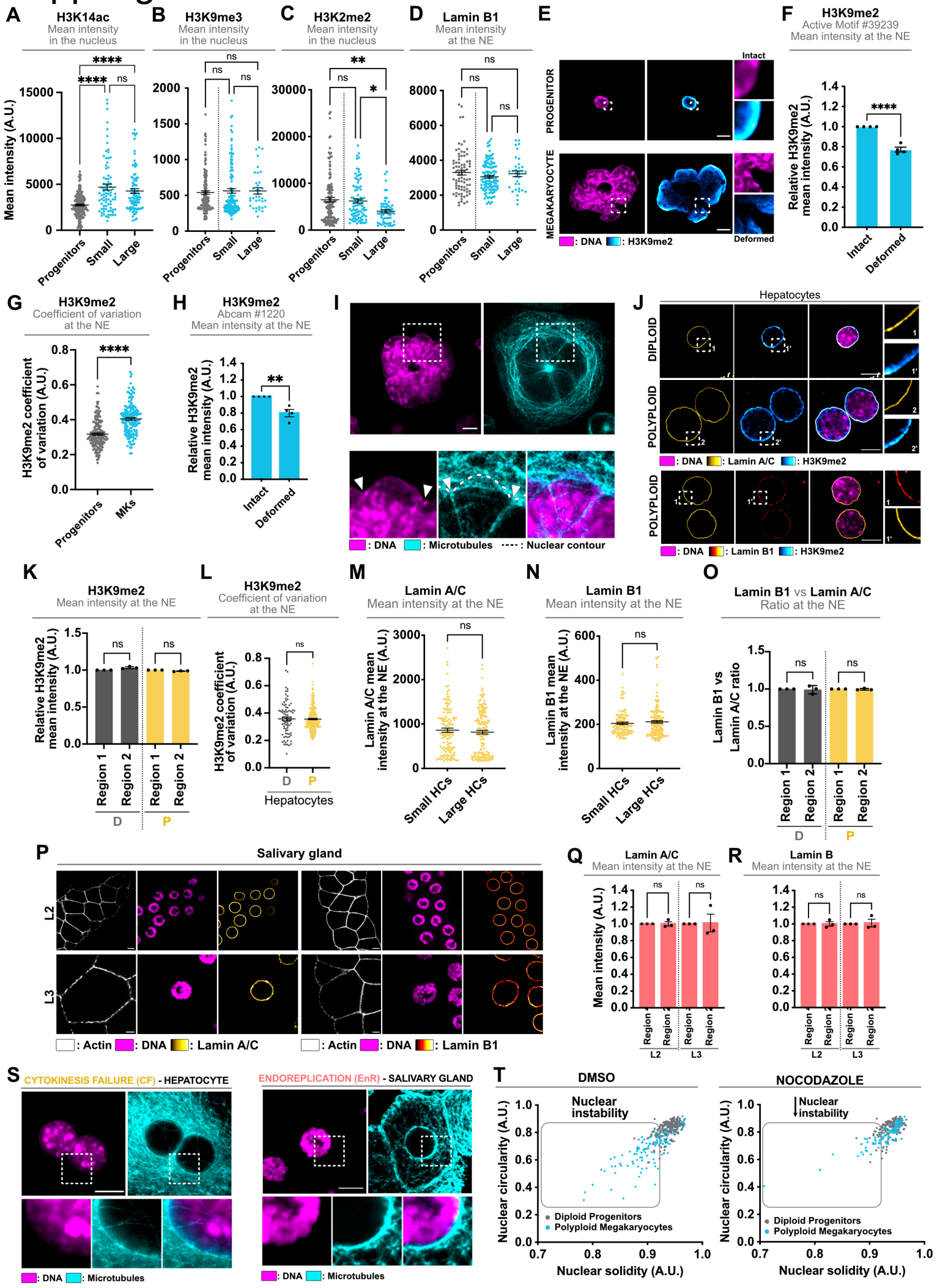
Supp Figure 10